5. THE ARCTIC—M. O. Jeffries and J. Richter-Menge, Eds.

a. Overview—M. O. Jeffries and J. Richter-Menge

The Arctic chapter describes observations of a variety of physical variables that encompass the atmosphere, ocean, and land. There were strong spatial and temporal contrasts in a number of variables during 2013. Illustrating the influence of significant interannual variability, some variables were similar to what was observed in 2012, while others were very different.

The mean annual air temperature in 2013 over the Arctic land area was similar to that of 2012, and it was the seventh warmest year observed in the Arctic since records began in the early 20th century. Negative (cold) winter air temperature anomalies across Eurasia were followed by positive (warm) spring air temperature anomalies, which were linked to a new record low Eurasian snow cover extent in May and early (3–4 weeks) lake ice break-up. Across the Arctic Ocean, low spring air temperatures extended from Iceland through Greenland and northern Canada to Alaska, which experienced its coldest April since 1924. Despite the relatively cool North American spring, snow cover extent in June was well below average.

The rate of snow cover loss over Northern Hemisphere land areas in June between 1979 and 2013 was –19.9% decade[-1] (relative to the 1981–2010 average). This exceeds the rate of September sea ice loss over the same time period (–13.7% decade[-1]), adding further compelling evidence of the observed rapid response of both the terrestrial and marine cryosphere to Arctic amplification in surface temperature trends.

Minimum sea ice extent in September was 1.69 million km[2] higher than the record minimum of 2012, yet it was still 1.12 million km[2] (18%) below the 1981–2010 average and the sixth lowest minimum extent since satellite observations began in 1979. A similar contrast between 2013 and 2012 conditions occurred on the Greenland ice sheet, where melting in 2013 was detected over 44% of the surface; a much lower value than the record 97% melt extent of 2012. The ice-sheet-wide albedo in 2013 was the highest since 2008, and the surface mass balance along the K-transect in west Greenland was much closer to the 1990–2010 average than it was in 2012.

Summer 2013 was characterized by a positive North Atlantic Oscillation, which gave rise to persistent low pressure over Greenland and adjacent regions, positive air temperature anomalies in western Eurasia, and a large area of anomalously low air temperatures stretching from Greenland through the high Canadian Arctic and across the Arctic Ocean to eastern Eurasia. As well as influencing sea ice extent and Greenland ice sheet melting, these conditions likely contributed to stronger cyclonic forcing over the Canada Basin, where the freshwater content of the upper ocean decreased by 7% and very little multiyear ice drifted into the Beaufort Sea north of Alaska and beyond into the East Siberian Sea.

Adjacent to the Beaufort Sea, new record high temperatures at 20-m depth were measured at some permafrost observatories on the North Slope of Alaska and in the Brooks Range. Permafrost temperatures also continued to rise elsewhere in the Arctic, including Canada, Russia, and the Nordic region. Atmospheric CO_2 and CH_4 concentrations increased by 3.2 ppm and 5.0 ppb, respectively, between 2012 and 2013. Each value is the same as the global increase during the same period, consistent with Arctic atmospheric CO_2 and CH_4 increases being due to export from lower latitudes rather than a consequence of increases in Arctic sources, e.g., thawing permafrost.

An unusually early stratospheric sudden warming event in January 2013 halted chemical destruction of ozone in the atmosphere. Consequently, the minimum total ozone column in March (414 Dobson Units) was 35% higher than the record minimum of 2011 and 13% higher than the 2000–10 average. Because of the above-average ozone levels in spring 2013, UV levels measured in the high Arctic were below the climatological mean for prolonged periods at several measurement sites.

b. The lower atmosphere: air temperature, clouds and surface radiation—J. Overland, J. Key, E. Hanna, I. Hanssen-Bauer, B.-M. Kim, S.-J. Kim, J. Walsh, M. Wang, U. Bhatt, Y. Liu, R. Stone, C. Cox, and V. Walden
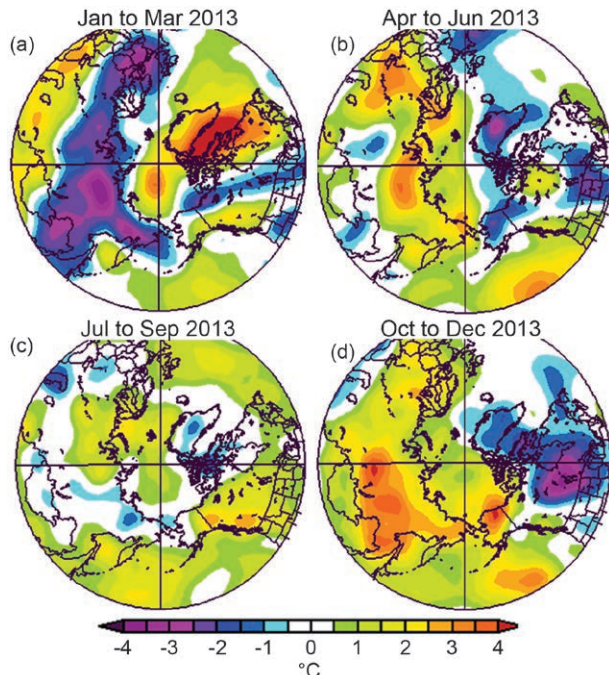
1) MEAN ANNUAL SURFACE AIR TEMPERATURE

The mean annual air temperature in 2013 was similar to 2012 and the seventh warmest year observed in the Arctic since records began in the early 20th century (Fig. 5.1). The first 13 years of the 21st century (2001–13) were about 1.0°C warmer than the last 20 years of the 20th century (1981–2000). Decadal-long, positive (warm) anomalies occurred in all parts of the Arctic, an indication that the early 21st century temperature increase is due to global warming rather than natural regional variability (Overland 2009). The temperature increase in the Arctic—more than double that observed at lower latitudes—is a manifestation of "Arctic Amplification" (Overland et al. 2011; Stroeve et al. 2012).
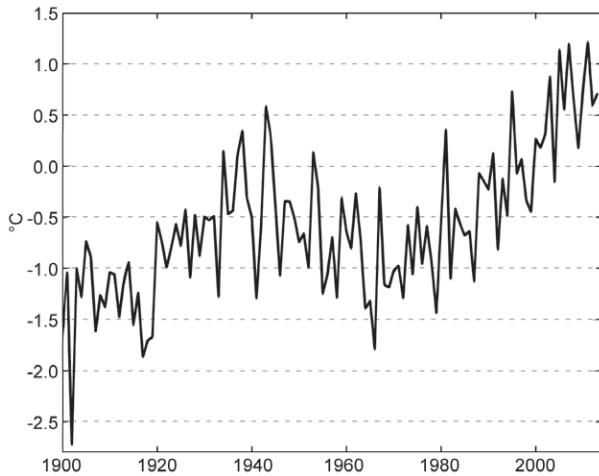
Fig. 5.1. Arctic-wide annual mean surface air temperature anomalies (°C) for land stations north of 60°N for the period 1900–2013 relative to 1981–2010 base period. (Source: CRUTEM4 dataset, http://www.cru.uea.ac.uk/cru/data/temperature/.)

2) Seasonal and regional surface air temperature variability

The annual mean air temperature in 2013 (Fig. 5.1) was influenced by positive and negative variability in seasonal and regional anomalies. (Fig. 5.2).

Fig. 5.2. Seasonal near-surface air temperature anomalies (°C) in 2013 relative to the 1981–2010 base period in (a) winter (Jan–Mar), (b) spring (Apr–Jun), (c) summer (Jul–Sep), and (d) fall (Oct–Dec). Temperature analyses are from slightly above the surface layer (at 925-hPa level), which emphasizes large spatial patterns rather than local features. (Source: NOAA/ESRL, http://www.esrl.noaa.gov/psd/.)

In winter 2013, Alaska enjoyed above-normal temperatures (Fig. 5.2a). The Arctic Basin also remained anomalously warm. A strong winter high temperature anomaly developed over the Baffin Bay region, with record high temperatures in March along the coast of west Greenland (see section 5j). In contrast, winter was particularly cold in Eurasia, from Scandinavia across the continent to easternmost Siberia (Fig. 5.2a).

In spring, the temperature anomaly pattern (Fig. 5.2b) was almost the opposite of the winter pattern. An area of anomalously low temperatures stretched from Iceland through Greenland and northern Canada to Alaska. Interior Alaska experienced its coldest April since 1924 and budburst/green-up of birch and aspen was the latest (26 May) since observations began in 1972 (Alaska Climate Research Center 2013). In contrast, anomalously high temperatures occurred over much of the Arctic Basin and Eurasia (Fig. 5.2b). The temperature anomalies observed in winter and spring 2013 were consistent with large-scale pressure and atmospheric circulation patterns, where positive 850-hPa geopotential height anomalies occurred in winter (Fig. 5.3a) and negative anomalies occurred in the spring (Fig. 5.3b). The 850-mb level winds give the large-scale circulation pattern that controls most of the lower level temperature field. Clockwise (anticyclonic) atmospheric circulation in winter (Fig. 5.3a) in the Atlantic Arctic advected colder air into Asia and warmer Atlantic air into northeastern North America. In spring (Fig. 5.3b), the atmospheric circulation reversed, with warmer air in particular being advected into Eurasia, where record low snow cover extent occurred in May (see section 5h). The change in atmospheric circulation between winter and spring (Fig. 5.3a,b) corresponded
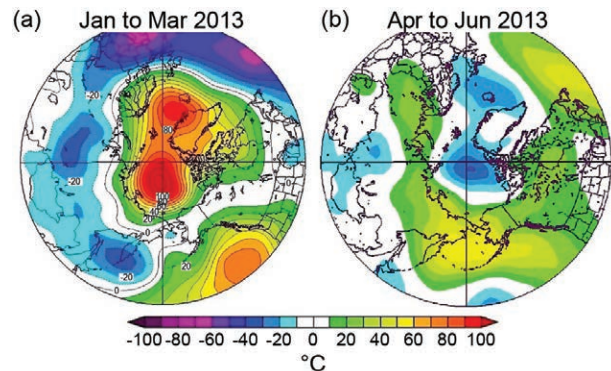
Fig. 5.3. The 850-mb geopotential height anomalies for (a) Jan–Mar and (b) Apr–Jun. The anomalies are calculated relative to the 1981–2010 average for each period. (Source: National Centers for Environmental Prediction.)

to a shift in the Arctic Oscillation, from negative in winter, especially in March, to positive in the spring.

Summer 2013 remained anomalously warm in Eurasia (Fig. 5.2c) and in Alaska, where an abrupt transition in late May to much-above normal temperatures heralded one of the hottest summers on record. For example, Fairbanks, in the Interior, experienced a record 36 days with maximum temperatures of 27°C or higher. In contrast to Eurasia and Alaska, anomalously low temperatures occurred over northernmost Canada and Greenland (Fig. 5.2c).

The relative coolness of Greenland, northernmost Canada, and the adjacent high Arctic Ocean in summer 2013 (Fig. 5.2c) is particularly evident when air temperature is compared to that of the period 2007–12 (Fig. 5.4a), when the six lowest minimum sea ice extents in the satellite record occurred (see section 5f; Perovich et al. 2013). Air temperatures across a broad swath of the Arctic Ocean in 2013 were 1°–3°C lower than during 2007–2012 and associated with a geographically extensive, but weak low pressure field (Fig. 5.4b). The relatively low temperatures are consistent with the increase in the minimum extent of the 2013 summer sea ice cover, relative to the record low in 2012 (see section 5f). Similarly, 1°–2°C lower temperatures over Greenland in summer 2013 (Fig. 5.4a) contributed to lower surface melt extent and duration, surface mass balance, and river discharge than recent years (see section 5j).

Fall temperatures (Fig. 5.2d), with positive temperature anomalies over the central Arctic, show typical conditions of the last decade related to reduced sea ice cover. This is the Warm Arctic–Cold Continent pattern of cold continental temperatures over northeastern North America associated with warm central Arctic temperatures, similar to 2009, 2010, and 2012 (Overland et al. 2011).

3) Cloud cover and surface radiation budget

Winter 2012/13 was characterized by below-average cloud cover over the western Arctic Ocean, particularly in January (Fig. 5.5a) and February, when cloud cover was 20% below the 2002–11 average. In contrast, early summer cloud cover in the same region was 15%–20% above average (Fig. 5.5b). As with the surface temperature anomalies, the cloud cover anomalies were consistent with large-scale pressure and atmospheric circulation patterns (see Fig. 5.3). Positive wintertime geopotential height anomalies and anticyclonic (high pressure) circulation, as was the case from January through March over the western Arctic Ocean, generally result in less cloud cover, while negative anomalies are associated with increased cyclonic activity and greater cloud cover (Liu et al. 2007). Over the Arctic Ocean, clouds radiatively warm the surface during winter and cool the surface in mid-summer. This relationship has been observed with surface measurements during the SHEBA experiment (Intrieri et al. 2002) and at Barrow, Alaska (Stone 1997), and with satellite data on a broader scale (Wang and Key 2005). The effect of the observed 2013 cloud cover anomalies on the surface radiation budget is one of decreased net longwave radiation during mid-winter, which results in radiative cooling at the surface, and decreased solar insolation during early summer, which also results
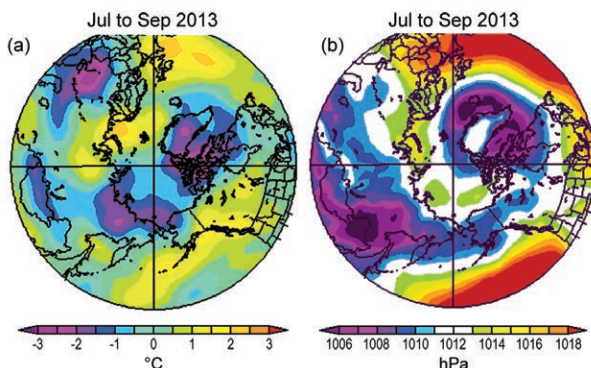
FIG. 5.4. (a) Near-surface air temperature (°C) anomalies for summer (Jul–Sep) 2013 relative to the 2007–12 average. (b) Mean sea level pressure (hPa) field for summer (Jul–Sep) 2013. Temperature analyses are from slightly above the surface layer (at 925-hPa level) which emphasizes large spatial patterns rather than local features. (Source: NOAA/ESRL, http://www.esrl.noaa.gov/psd/.)
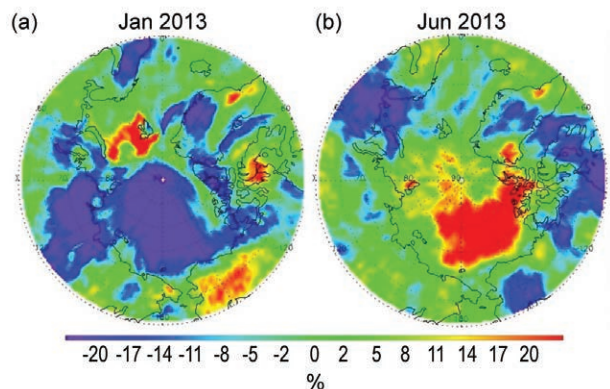
FIG. 5.5. Cloud cover anomalies (%) in (a) Jan and (b) Jun 2013. The anomalies are calculated relative to the 2002–11 average for each month from observations by the Moderate Resolution Imaging Spectroradiometer (MODIS) on the Aqua satellite. [Source: MODIS L1 and Atmosphere Archive and Distribution System (LAADS).]

The sea ice cover on the Arctic Ocean is dwindling, particularly in summer, spring snow on Arctic land areas is disappearing earlier, the Greenland ice sheet is losing mass, and other signs of a dramatically warming Arctic are emerging. Loss of ice and snow, among other factors, amplifies global temperature changes through numerous positive feedbacks that make the Arctic more sensitive to change than any other region on Earth. In recent decades the Arctic has warmed at least twice as fast as the rest of the Northern Hemisphere. Recent studies suggest that the rapidly warming Arctic may be linked to observed extreme weather events, such as cold spells (Tang et al. 2013a; Cohen et al. 2013) and heat waves (Tang et al. 2013b) in Northern Hemisphere continents, as well as wet summers in western Europe (Screen 2013). However, the mechanisms that connect Arctic warming to extreme weather at lower latitudes remain elusive.

The disproportionate high-latitude warming, known as Arctic amplification, may have significant impacts on the large-scale atmospheric circulation of the Northern Hemisphere because the difference in temperature between the Arctic and midlatitudes is a fundamental driver of the polar jet stream. When the temperature difference is large, the westerly winds of the jet stream tend to be strong and its path is relatively straight around the hemisphere. When the difference is smaller, the upper-level zonal flow weakens and tends to meander more with larger north–south excursions (Thompson and Wallace 2001; Palmén and Newton 1969). Arctic amplification causes the thickness of atmospheric layers to increase more in the north, leading Francis and Vavrus (2012) to hypothesize that the peaks of ridges should elongate northward and thus further increase the north–south amplitude of the flow's waviness. Weaker zonal winds owing to the reduced poleward temperature difference cause waves to travel eastward more slowly; thus, Arctic amplification should retard the progression of large-scale atmospheric waves, leading to more persistent weather patterns.

Some links in this hypothesized chain of events are clearly observed in the real world and in model simulations, but the emergence only recently of Arctic amplification amid the noise of natural variability (Fig. SB5.1) limits detection of its effects on the midlatitude circulation, contributing to the lack of statistically significant circulation changes (Screen and Simmonds 2013). Arctic amplification is largest in fall and winter, owing primarily to feedbacks involving sea-ice loss and increased atmospheric water vapor (Screen and Simmonds 2010); thus, the atmospheric response should become evident first and be largest in cold seasons. Indeed, a significant decrease in zonal-mean wind at 500 hPa during fall (October–December) is apparent (Fig. SB5.2; see also figure 4a in Barnes 2013). In other seasons, when Arctic amplification is weaker (spring and summer) and/or less concentric around the pole (winter), the areas of weaker zonal winds coincide with regions where the poleward temperature gradient has declined. Anomalies in the 1000–500 hPa thickness in and zonal winds for winter (January–March) shown in Fig. SB5.3 illustrate this behavior. This suggests that as Arctic amplification strengthens in all seasons, the zonal wind reduction and its effects on weather patterns will become more pronounced.
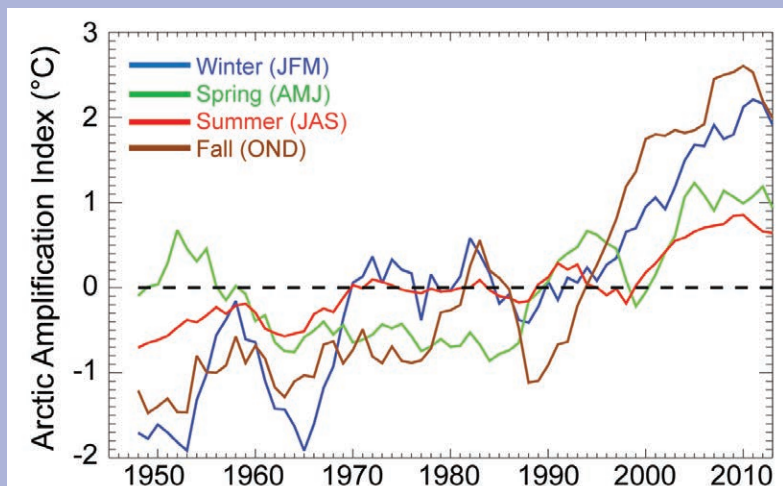
FIG. SB5.1. Five-year running mean time series of seasonal-mean Arctic amplification, calculated as the difference in air temperature anomalies (°C, relative to 1948–2013 average) at 1000 hPa between the Arctic (70°–90°N) and midlatitudes (30°–70°N). (Source: NOAA/ESRL, http://www.esrl.noaa.gov/psd/.)
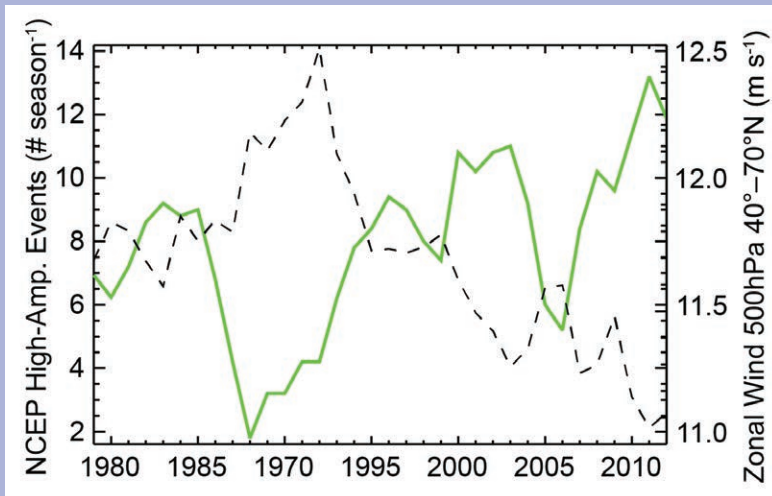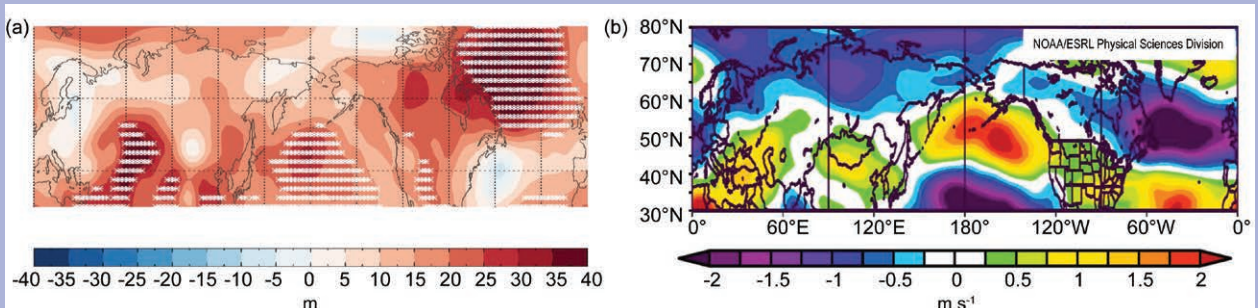
FIG. SB5.2. Five-year running mean of high-amplitude (>35°N latitude) wave events (days season⁻¹) during fall in the NH (green line) based on the daily maximum/minimum latitude difference of the 5600-m height contour of the 500-hPa pressure level. The black dashed line is the corresponding zonal-mean zonal wind speed (m s⁻¹) at 500 hPa between 40°–70°N. Note the general anti-correlation between the two data sets (r = -0.68). (Source: NCEP/NCAR reanalysis, http://www.esrl.noaa.gov/psd/.)

variability of the atmosphere. However, recent studies provide some supporting evidence of these responses during fall and summer (e.g., Screen and Simmonds 2013; Francis and Vavrus 2012). A significant reduction in 500-hPa wave speeds during fall was reported by Barnes (2013), but the response was not apparent in higher-level winds. Although the frequency of blocking-high patterns has not been increasing consistently since 1979 across all seasons, regions, and different measurement techniques (Barnes et al. 2014), high-amplitude upper-level patterns (not necessarily blocking highs) do appear to be increasing in the Northern Hemisphere during fall (Fig. SB5.2), particularly during the past two decades, when Arctic amplification has become more pronounced, and 500-hPa zonal winds have decreased by approximately 10%.

Much research is still needed to understand better the mechanisms by which midlatitude weather patterns will respond to the changing climate system, and particularly if and how they may be affected by Arctic amplification. There is also much to learn about the interplay among Arctic amplification and modes of natural variability (such as ENSO, the PDO, and AMO), as well as the behavior and trends in weather patterns by region and season as the Earth and the Arctic experience unabated warming.

Support for the rest of the Francis and Vavrus (2012) hypothesis is less solid—namely, whether a weaker zonal flow leads to larger amplitude waves, slower wave propagation speeds, and more persistent weather patterns. Statistically robust evidence of increasing north–south wave amplitude and slower propagation speed has not been established, which is not surprising given the emergence only recently of Arctic amplification and the large natural

FIG. SB5.3. Anomalies (relative to 1981–2010 average) in (a) 1000–500-hPa thickness (m) and in (b) 500-hPa zonal winds (m s⁻¹) for winter during 2000–12. White asterisks in (a) indicate >95% confidence in difference from the mean. (Source: NCEP/NCAR reanalysis, http://www.esrl.noaa.gov/psd/.)

in surface cooling. This can be seen in the field of January net radiation at the surface (Fig. 5.6a). Above-average surface radiation loss prevailed over most of the Arctic Basin during the month, centered in the region of the Laptev, East Siberian, and Chukchi Seas, where the negative cloud anomaly was also centered. There is also empirical evidence of a decrease in net radiation in response to reduced cloud cover (Fig. 5.5a) at the NOAA Baseline Observatory in Barrow, Alaska. During January 2013, there was a reduction in net surface radiation of approximately 12 W m^{-2} (Key et al. 2013) in response to a −18% sky cover anomaly relative to the 2002–11 average. The January net radiation anomalies are consistent with the cloud cover anomalies throughout most of the Arctic such that decreased cloud amounts resulted in decreased (more negative) net radiation from radiative cooling. In June, below-average net surface radiation corresponds to above-average cloud cover over and northwestward of the Canadian Arctic Archipelago (Figs. 5.5b, 5.6b), where downwelling solar radiation is reduced by cloud cover. Over the central Arctic Ocean, the surface temperature anomaly in June was near zero or slightly positive, as was the surface net radiation anomaly. In much of this area the cloud cover was up to 20% above average, implying a neutral cloud forcing, with shortwave and longwave cloud effects similar in magnitude but opposite in sign, offsetting one another. Overall, the cloud radiative effect on the surface energy budget was larger in January than in June. The influence of the January–February cloud anomaly on the September 2013 ice extent is discussed in Liu and Key (2014).
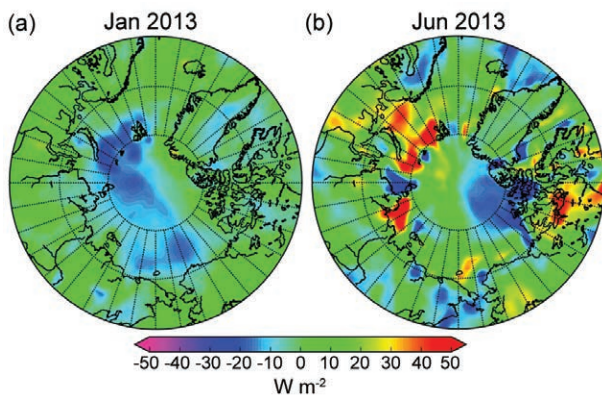

Fig. 5.6. (a) Jan and (b) Jun 2013 net radiation (W m^{-2}) anomalies at the surface (net longwave plus net short-wave) derived from ERA-Interim (Dee et al. 2011). A positive anomaly indicates that the surface is gaining energy, and vice-versa. The anomalies are calculated relative to the 2002–11 average for each month, consistent with the cloud anomalies in Fig. 5.5.

c. Arctic ozone—G. Bernhard, G. Manney, V. Fioletov, J.-U. Grooß, and R. Müller

The total ozone column in the Arctic measured by satellites and ground-based instruments during spring 2013 exceeded the average of the last decade. The minimum total ozone column for March, averaged over the "equivalent latitude" (Butchart and Remsberg 1986) band 63°–90°N, was 414 Dobson Units (DU). This value is 47 DU above the most recent decadal average (2000–10) of 367 DU, 17 DU above the earlier historical period (1979–88) of 397 DU and comparable to observations in previous warm winters that did not have significant ozone depletion (e.g., 1999, 2001, and 2006; Fig. 5.7). The record minimum of the satellite era was 308 DU, set in 2011.

With few exceptions, in 2013 there were no extended areas with large (>10%) deviations of the monthly mean total ozone column from the historical (1979–1988) mean (Bernhard et al. 2013a, figure 11). Exceptions include a region with elevated (~10%) total ozone over northern Scandinavia in February. In March, areas with total ozone more than 10% below average were observed over northern Canada and the North Pole, while positive anomalies of similar magnitude were centered over the Kola Peninsula, Russia, and northern Scandinavia. Monthly anomalies for April remained within ±10% of average throughout the Arctic. Average total ozone for May over Iceland was elevated by about 15%.
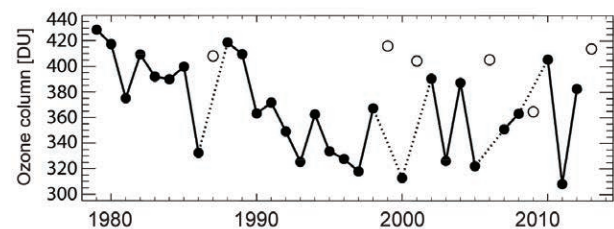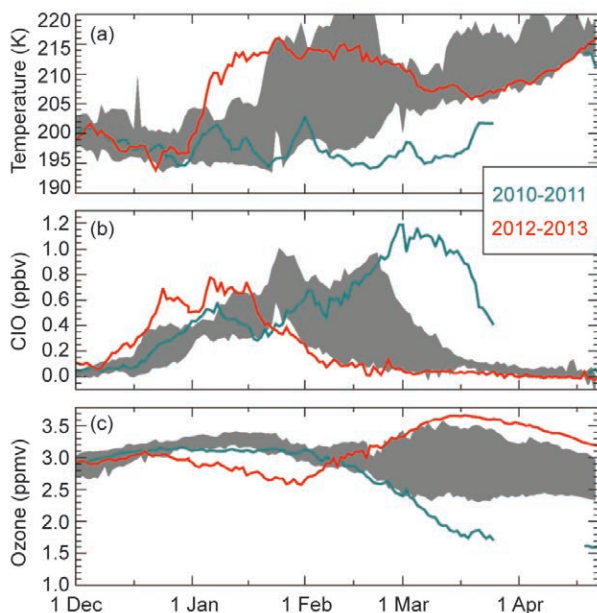

Fig. 5.7. Time series of area-averaged minimum total ozone for Mar in the Arctic, calculated as the minimum of daily average column ozone poleward of 63°N equivalent latitude. Open circles are also for Mar, but represent years in which the polar vortex broke up before Mar. Ozone in those years was relatively high because of mixing with air from lower latitudes and higher altitudes, and the lack of significant chemical ozone depletion. [Source: adapted from Müller et al. (2008), updated using ERA-Interim reanalysis data (Dee et al. 2011). Ozone data from 1979–2012 are based on the combined total column ozone database produced by Bodeker Scientific (http://www.bodeker-scientific.com/data/total-column-ozone); 2013 data are from the Ozone Monitoring Instrument aboard the NASA Aura satellite.]

The relatively high ozone concentrations in 2013 compared to those observed during the last decade resulted from a large increase in stratospheric temperatures during the first half of January 2013 (Fig. 5.8a). Similar "stratospheric sudden warming" (SSW) has occurred in late winter and early spring in many years of the last two decades, but is less common for early January. The early winter timing of the SSW in January 2013 halted the chemical destruction of ozone in the stratosphere. The contrast between the meteorological conditions in 2012/13 with those in 2010/11, when a persistently cold stratosphere and prolonged high chlorine activation caused severe ozone destruction, highlights the large range of interannual variability in Arctic winter conditions, and hence in Arctic ozone (Fig. 5.7).

The temporal evolution of several variables that were crucial for the rate and extent of stratospheric ozone loss during the winter/spring of 2012/13 is illustrated in Fig. 5.8. Stratospheric temperatures in December 2012 were among the lowest on record (Fig. 5.8a). Low temperatures, below about 195 K (–78°C), facilitated the formation of polar stratospheric clouds (PSC), which occur at altitudes between about 15 and 25 km. Chemical reactions on PSC cloud particles transform inactive forms of chlorine, such as chlorine nitrate ($ClONO_2$) and hydrogen chloride (HCl), to active, ozone-destroying forms of chlorine such as chlorine monoxide (ClO). The conversion of inactive to active forms is indicated by the increase in ClO (Fig. 5.8b) following the start of PSC occurrence. ClO concentrations remained elevated for about one month after the start of the SSW event.

Ozone destruction occurs as long as chlorine is activated in regions that experience sunlight. Even with chlorine activated, ozone destruction is typically small in December and January when the polar regions are in darkness. Owing to the large SSW event, the polar vortex in late 2012 and early 2013 was shifted away from the North Pole and was exposed to more sunlight than usual. The steady decrease in ozone between late December and late January (Fig. 5.8c) indicates that significant chemical ozone loss occurred.

Chlorine was finally deactivated in early February (Fig. 5.8b) and ozone increased, primarily because of an influx of ozone from higher altitudes. After mid-February, ozone concentrations in the Arctic stratosphere were the highest since 2005 (Fig. 5.8c). Thus, the SSW in January and the associated rise in stratospheric temperatures prevented extensive ozone losses in 2013, in stark contrast to the situation in 2011, when low temperatures persisted into spring, resulting in unprecedented ozone destruction during that year (Manney et al. 2011).

FIG. 5.8. Averages of (a) high-latitude stratospheric temperatures (K), (b) chlorine monoxide (ppbv), and (c) ozone (ppmv) from NASA Aura Microwave Limb Sounder measurements. Observations during the 2012/13 Arctic winter (red lines) are compared with similar data from the 2010/11 Arctic winter (blue-green lines), when unprecedented chemical ozone loss occurred. Gray shading indicates the range of values observed between winter 2004/05 and winter 2011/12 (excluding the extreme minimum of 2010/11 when the first ever Arctic ozone hole was observed). Temperature and mixing ratios refer to the 485 K potential temperature surface (altitude of ~18 km) and were averaged over the area of the stratospheric polar vortex.

d. UV radiation—G. Bernhard, V. Fioletov, A. Heikkilä, B. Johnsen, T. Koskela, K. Lakkala, T. Svendby, and A. Dahlback

Ultraviolet radiation, expressed here as the UV Index (UVI), is a measure of the ability of UV radiation to cause erythema (sunburn) in human skin (WHO 2002; McKinlay and Diffey 1987). In addition to the total ozone column (see section 5c), the UVI depends greatly on the sun angle and cloud cover, as well as other factors (Weatherhead et al. 2005) such as aerosols (liquid and solid particles suspended in air) and surface conditions (e.g., snow and ice cover). In the Arctic, the UVI scale ranges from 0 to about 7, with sites closest to the North Pole having the smallest peak radiation and UVI values <4 all year. UVI

values <5 indicate low to moderate risk of erythema (WHO 2002).

At high latitudes, satellite-based estimates of the surface UVI are subject to large uncertainties because it is difficult to distinguish snow and ice reflectivity (which increases the UVI) from cloud reflectivity (which decreases the UVI) with current space-borne sensors (Tanskanen et al. 2007; Ialongo et al. 2011; Herman et al. 2013). UV radiation is, therefore, assessed with ground-based instruments that are deployed at latitudes between 60° and 83°N in Canada, Alaska, the center of the Greenland ice sheet, Svalbard, Norway, and Finland. Because of the above-average ozone amounts observed in spring 2013 (see section 5c) UV levels measured in the high Arctic were below the climatological mean for prolonged periods at several stations. However, the timing of these low-UV episodes was not uniform across the Arctic. For example at Alert, at 83°N in the Canadian high Arctic and approximately 700 km from the North Pole, the UVI remained continuously below the climatological mean between 28 April and 27 May 2013 (Fig. 5.9a). In contrast, UVI measurements at Ny-Ålesund, in the Svalbard archipelago north of Scandinavia and approximately 1000 km from the North Pole, were below the climatological mean during February and March 2013 when absolute UVI values were below 1 (Fig. 5.9b).

UV intensities in southern Scandinavia were mostly controlled by cloud variability and UV levels in 2013 remained within the range of historical (1995–2012) measurements. Enhanced UV levels were observed in northern Scandinavia during May and early June. For instance, UV levels at Sodankylä, at 67°N in northern Finland, were close to historical maxima between 16 May and 7 June 2013 (Fig. 5.9c), and, on average, the UVI was elevated by 38% compared to the climatological mean. The enhancement was mostly caused by low cloudiness, but satellite observations provided by the Tropospheric Emission Monitoring Internet Service (TEMIS, http://www.temis.nl/) indicate that advection of low-ozone air from lower latitudes was also a contributing factor.

Clouds lead to a large variability in UV levels on time scales of minutes to days, but the effect is largely reduced when the ground is covered by fresh snow (Bernhard et al. 2008). Measurements at Alert (Fig. 5.9a), and to a lesser extent at Ny-Ålesund (Fig. 5.9b), show a large asymmetry between spring (low variability) and fall (high variability) because the
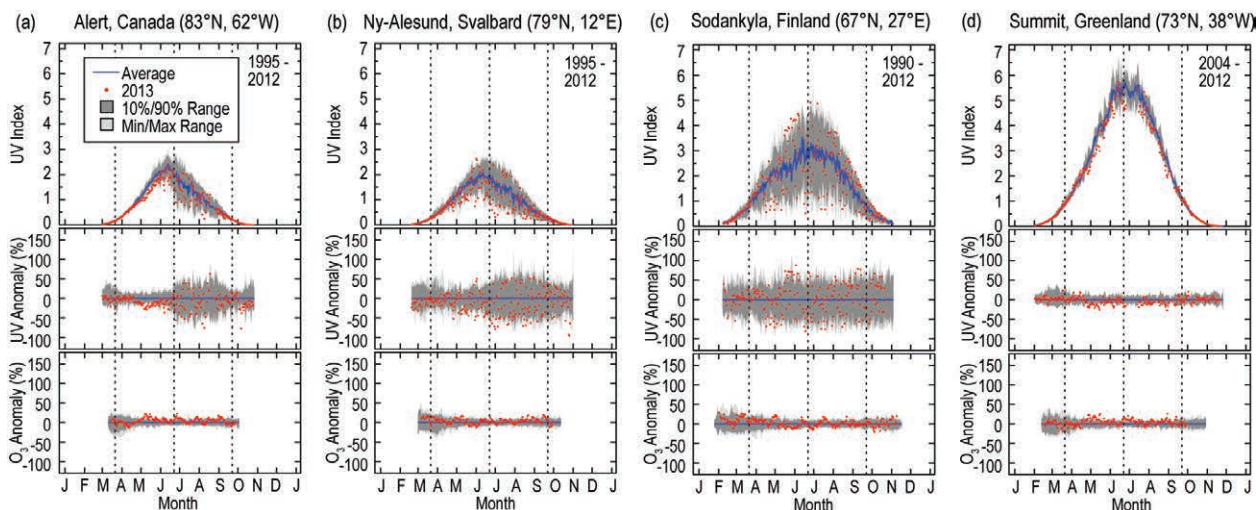
Fig. 5.9. Seasonal variation of the UV index (UVI) measured by ground-based radiometers at (a) Alert, Canada, (b) Ny Ålesund, Svalbard, Norway, (c) Sodankylä, Finland, and (d) Summit, Greenland. Data are based on the UVI averaged over a 2-hr period centered at solar noon. The top panel for each site compares UVI in 2013 (red dots) with the average noontime UVI (blue line), the range between the 10th and 90th percentile (dark shading), and the range of historical minima and maxima (light shading). Average (climatological mean) and ranges were calculated from measurements of the years indicated in the top-right corner of each UVI panel. The center horizontal panel shows the relative UVI anomaly calculated as the percentage departure from the climatological mean. The bottom panel shows a similar anomaly analysis for total ozone derived from measurements of the following satellites: TOMS/Nimbus7 (1991–92), TOMS/Meteor3 (1993–94), TOMS/EarthProbe (1996–2004), and OMI (2005–13). The shaded ranges for the ozone data set are based on data for 1991–2012. Ozone data are available at http://avdc.gsfc.nasa.gov/index.php?site=1593048672&id=28 and http://ozoneaq.gsfc.nasa.gov. Vertical broken lines indicate the vernal equinox, summer solstice, and autumnal equinox. Additional geographical and meteorological information for the four locations is provided by Bernhard et al. (2013b).

surface at these sites is covered by snow until about June and free of snow thereafter until the beginning of the following winter. In addition, the sky at Alert is mostly clear in the spring while clouds are prevalent in the summer. The location of Summit Station (Fig. 5.9d), close to the center of the Greenland ice sheet, is snow-covered year-round and the variability introduced by clouds is thus small. The well-known anti-correlation between total ozone and the UVI (Weatherhead et al. 2005) is therefore not masked by cloud variability at this site. For example, the UVI at Summit Station remained continuously below the mean between 26 April and 19 May 2013—with UVI measurements dropping below historical (2004–12) minima on several days—when the ozone column was elevated (Fig. 5.9d).

e. Carbon dioxide and methane—L. Bruhwiler, E. J. Dlugokencky, T. Laurila, and D. Worthy

Atmospheric carbon dioxide (CO_2) and methane (CH_4) are responsible for ~82% of increased direct radiative forcing by long-lived greenhouse gases since 1750; in 2012 this amounted to 2.35 out of 2.87 W m^{-2} (see http://www.esrl.noaa.gov/gmd/aggi/, an update of Hofmann et al. 2006). Natural emissions of these gases are of particular interest in the Arctic where there are large vulnerable reservoirs of carbon in soil and clathrates that may eventually be released to the atmosphere by thawing and decomposition. Since the mobilization of Arctic soil carbon is expected to increase with rising air temperatures, it might act as a positive feedback on global climate. Detection of trends in greenhouse gas emissions from Arctic sources is difficult, however, because the changes are expected to be small in comparison to the much larger midlatitude and tropical emissions that are transported to the Arctic atmosphere.

Current understanding of CO_2 and CH_4 in the Arctic atmosphere is based on in situ measurements by national monitoring programs. Currently, CO_2 and CH_4 data are available for 16 Arctic sites (Fig. 5.10; Table 5.1) maintained by NOAA, Environment Canada, the Finnish Meteorological Institute, and collaborators in Norway and Iceland. The longest time

Fɪɢ. 5.10. Locations of high northern latitude sites where atmospheric CO_2 and CH_4 are monitored.

series are from Barrow, Alaska, US (1983–present) and Alert, Nunavut, Canada (1985–present). In recent years, more sites have been added, including Pallas, Finland (2002–present) and several new sites in the Canadian Arctic. Maintaining long observational records is critical to timely detection of Arctic-wide trends in greenhouse gas emissions.

CO_2 and CH_4 measurements are generally made in one of two ways. Continuous, high-frequency measurements collected near local sources using in situ analyzers can improve understanding of regional processes that are responsible for surface-atmospheric exchange of CO_2 and CH_4. Discrete whole-air samples collected about weekly, then shipped to a central analysis laboratory, are useful for capturing Arctic-scale features in greenhouse gas concentration.

Table 5.1. List of high northern latitude sites where CO_2 and CH_4 are monitored. The year that CO_2 and CH_4 observations began is given in columns four and five.

Measurement Site	Lat.	Lon.	CO_2	CH_4
Alert, Nunavut, Canada	82°N	62°W	1985	1985
Barrow, Alaska, US	71°N	156°W	1971	1983
Behchoko, Northwest Territories, Canada	62°N	116°W	2010	2010
Cambridge Bay, Nunavut, Canada	69°N	105°W	2010	2010
CARVE Tower, Alaska, US	65°N	147°W	2012	2012
Cherskii, Russia	68°N	161°E		2008
Churchill, Manitoba, Canada	58°N	94°W	2007	2007
Cold Bay, Alaska, US	55°N	162°W	1978	1983
Inuvik, Northwest Territories, Canada	68°N	133°W	2012	2012
Pallas-Sammaltunturi, Finland	68°N	24°E	2001	2001
Shemya Island, Alaska, US	52°N	174°W	1985	1985
Storhofdi, Vestmannaeyjar, Iceland	63°N	20°W	1992	1992
Summit, Greenland	72°N	38°W	1997	1997
Teriberka, Russia	62°N	35°E	1998	1999
Tiksi, Russia	71°N	128°E	2010	2010
Zeppelin, Ny-Alesund, Svalbard, Norway	78°N	12°E	1994	1994

SIDEBAR 5.2: **RADIATIVE FORCING BY BLACK CARBON IN THE ARCTIC**—P. K. QUINN, A. STOHL, A. BAKLANOV, M. G. FLANNER, A. HERBER, K. KUPIAINEN, K. S. LAW, J. SCHMALE, S. SHARMA, V. VESTRENG, AND K. VON SALZEN

Black carbon (BC) is the most efficient atmospheric particulate species at absorbing visible light. Consequently, it exerts a warming effect that contrasts with the cooling effect of purely scattering aerosol components such as sulfate. However, pure BC particles rarely occur in the atmosphere. Soon after emission, BC becomes mixed with other components such as sulfate and organics. BC-containing particles can have either a warming or a cooling effect on climate depending on their altitude and the albedo of the underlying surface relative to the albedo of the BC haze itself. The albedo of the haze depends on the relative amounts of all of the chemical components present, their mixing state, and whether they primarily scatter or absorb light. BC-containing aerosols, unlike greenhouse gases, are short-lived, with a lifetime in the atmosphere on the order of days to weeks. While recognizing that reductions in CO_2 emissions are required for long-term mitigation of Arctic warming, it has been suggested that reducing emissions of BC could reduce projected global mean warming and slow the rate of warming in the short term in the Arctic (Shindell et al. 2012; Bowerman et al. 2013).

Atmospheric BC concentrations in the Arctic have declined since the 1990s (Sharma et al. 2013), and the BC content of Arctic snow is now no higher than it was thirty years ago (Clarke and Noone 1985; Doherty et al. 2010), but BC-containing aerosols will likely continue to influence Arctic climate through several different forcing mechanisms. Atmospheric BC can directly warm the Arctic atmosphere by absorbing solar radiation that would otherwise have been reflected back to space or absorbed by the surface (far right panel in Fig. SB5.4). The added atmospheric heating subsequently increases the downward longwave radiation to the surface and decreases the temperature difference between the surface and the atmosphere, thereby warming the surface. With the highly reflective snow and ice surfaces typical of the Arctic, even a moderately absorbing aerosol can lead to a heating of the surface–atmosphere column. The average daily radiative efficiency of atmospheric BC (units of W g^{-1}) in the Arctic summer is greater than in most other environments because of the long sunlight exposure and presence of highly reflective clouds, snow, and sea ice (e.g., Cess 1983). As summer progresses and open water appears within the sea ice cover, and melt ponds form

on the ice surface, the direct forcing efficiency by atmospheric BC decreases because the surface becomes less reflective. Similarly, it is reasonable to expect that forcing by atmospheric BC will become weaker as snow, sea ice, and glacier extent and surface albedo decrease under a warming climate (Flanner et al. 2009).

BC deposited to snow and ice surfaces enhances the absorption of solar radiation at the surface and warms the lower atmosphere, which can initiate snow and ice melt earlier in the season (left center panel in Fig. SB5.4). Even very low BC concentrations (ppb) of deposited BC have an impact because the absorptivity of BC is about five orders of magnitude greater than ice at visible wavelengths. In addition, multiple scattering in surface snow greatly increases the path-length of photons and the probability that they will encounter non-ice particles (Warren and Wiscombe 1980). Snow darkening drives an equilibrium temperature response, per unit of radiative forcing, several times that of CO_2 (Koch et al. 2009). This large impact occurs because all of the energy associated with the forcing is deposited directly into the snow and ice covers, components of the Earth system responsible for powerful positive feedback (e.g, Robock 1983; Hansen and Nazarenko 2004).

Radiative forcing by BC can also result from the impact of aerosols on cloud distributions, lifetime, and microphysical properties. By increasing the number of cloud droplets and decreasing cloud droplet size, aerosols can lead to an increase in reflectivity and cloud optical thickness (first indirect effect) and to an increase in cloud lifetime and a decrease in precipitation (second indirect effect; e.g., Twomey 1977). Both of these changes result in greater reflection of solar shortwave radiation back to space and a cooling at the surface (right center panel in Fig. SB5.4). In contrast, when the cloud droplet number concentration of thin Arctic liquid-phase clouds is increased through interaction with anthropogenic aerosols, the clouds become more efficient at trapping and re-emitting longwave radiation, which results in a warming at the surface (Garrett and Zhao 2006; far left column in Fig. SB5.4). BC can also impact clouds through semi-direct effects associated with atmospheric heating. Depending on circumstances, BC-induced heating can either stabilize the atmosphere and increase low-level cloud formation (Hansen et al. 2005), inhibit cloud formation, or increase
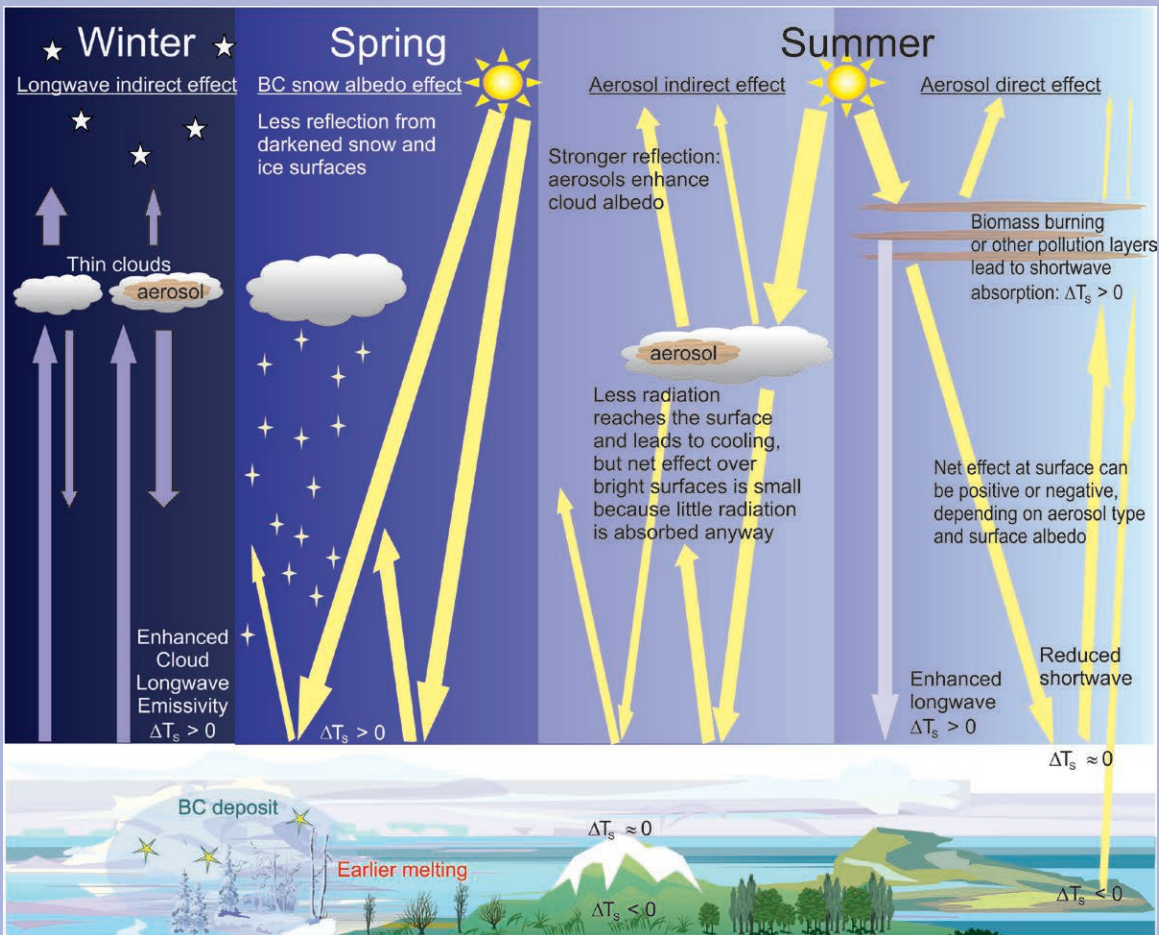
Fɪɢ. SB5.4. Forcing mechanisms in the Arctic due to black carbon. ΔT_s **indicates the surface temperature response.**

the evaporation rate of clouds (e.g., Ackerman et al. 2000; Jacobson 2010). Simulating these indirect and semi-direct effects remains a challenge for global-scale models, especially in the Arctic. Both the sign and magnitude of the net forcing due to nonlinear interactions between BC and clouds in the Arctic are uncertain.

Further complicating the impact of BC on Arctic climate is that forcing exerted by BC outside of the Arctic can result in changes in energy transport through the atmosphere and oceans to the Arctic (Shindell and Faluvegi 2009). For example, BC-heated air masses can travel from midlatitudes to the Arctic.
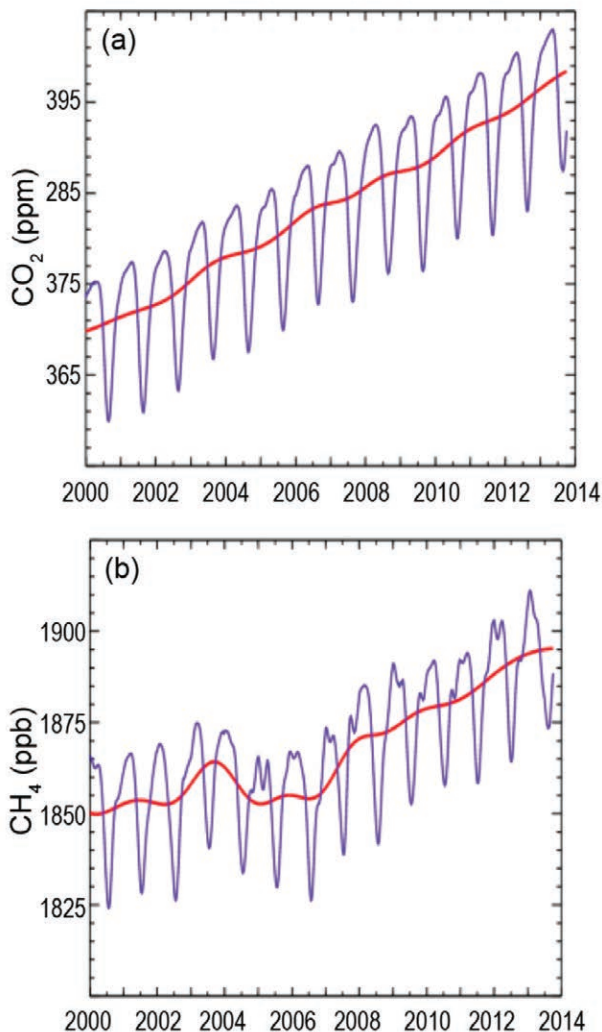
In the past few years there has been a concerted effort by the scientific community to quantitatively estimate the climate impacts of BC, both globally and within the Arctic

(e.g., Bond et al. 2013; Quinn et al. 2008). Currently, there is no single appropriate environmental indicator to assess the Arctic climate response to changes in emissions of BC and co-emitted species including organic carbon and sulfate. Hence, only an integrated evaluation will reduce the large uncertainties and improve estimates of BC's climate impacts. Such an evaluation requires accurate emission inventories of local and remote sources, long-term monitoring and process-oriented measurements, and global models capable of realistic transport of BC to the Arctic and depositional losses en route and within the Arctic. In addition, models must accurately capture feedbacks induced by BC, including those associated with snow, glacier, and sea-ice loss, cloud changes, and dynamical changes.

Measurements made by both approaches are typically calibrated with standards based on WMO mole fraction scales maintained at NOAA ESRL. Uncertainties estimated using a Monte Carlo method for the NOAA zonal means in Figs. 5.11a and 5.11b are 0.3–0.6 ppm for CO_2 and 2–4 ppb for CH_4 weekly averages.

Observations of atmospheric CO_2 (Fig. 5.11a) averaged for the Arctic observation sites show that CO_2 continued to increase in 2013 (3.2 ppm higher than in 2012, the same as the global increase). At present, trends in Arctic atmospheric CO_2 due to changes in Arctic productivity or respiration are difficult to distinguish from midlatitude anthropogenic emissions;

most of the increase in atmospheric CO_2 in the Arctic is from combustion of fossil fuels at midlatitudes.
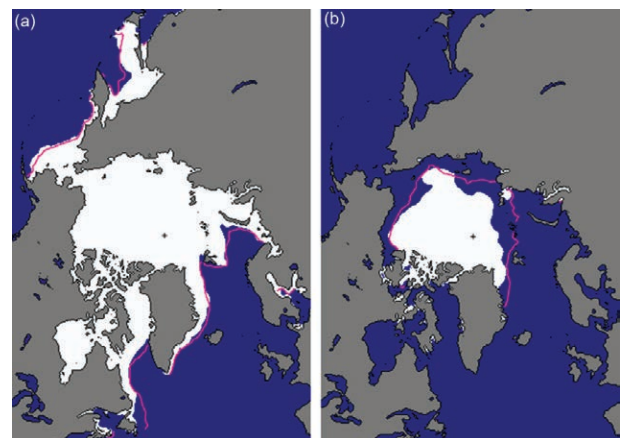
After a period of stability from 1999 to 2006 (the reasons for this are not fully understood and it is a topic of continuing research), CH_4 in the Arctic atmosphere began increasing in 2007 (Fig. 5.11b). In 2013, CH_4 was 5.0 ppb (preliminary estimate) higher than in 2012, equal to the increase in global CH_4. The increase in global CH_4 is attributed to a combination of increased tropical natural emissions and emissions from fossil fuel production, agriculture, and waste (Bruhwiler et al. 2014; Bergamaschi et al. 2013). Although interannual variability in Arctic emissions is captured in the Arctic observations, large sustained increases in CH_4 emissions from Arctic sources have not been observed.

f. Sea ice cover—D. Perovich, S. Gerland, S. Hendricks, W. Meier, M. Nicolaus, J. Richter-Menge, and M. Tschudi

1) SEA ICE EXTENT

Sea ice extent is a fundamental descriptor of the state of the Arctic sea ice cover. Satellite-based passive microwave instruments have been used to determine sea ice extent since 1979. There are two months each year that are of particular interest: September, at the end of summer, when the sea ice reaches its annual minimum extent, and March, at the end of winter, when the ice reaches its annual maximum extent. The sea ice extent in March 2013 and September 2013 are presented in Fig. 5.12.

Based on estimates produced by the National Snow and Ice Data Center (NSIDC), the sea ice cover reached a minimum annual extent of 5.10 million

FIG. 5.11. Weekly averages of (a) CO_2 (ppm) and (b) CH_4 (ppb) for 16 high northern latitude sites (blue curves) with deseasonalized trends (red curves). The seasonal CO_2 cycle reflects uptake by the terrestrial biosphere during the NH growing season and respiration during the winter months. The minimum in the CH_4 seasonal cycle occurs during the NH summer due to solar radiation-dependent photochemical destruction.

FIG. 5.12. Sea ice extent in (a) Mar and (b) Sep 2013, illustrating the respective monthly averages during the winter maximum and summer minimum extents. The magenta lines indicate the median ice extents during the period 1981–2010. (Source: NSIDC, http://nsidc .org/data/seaice_index.)
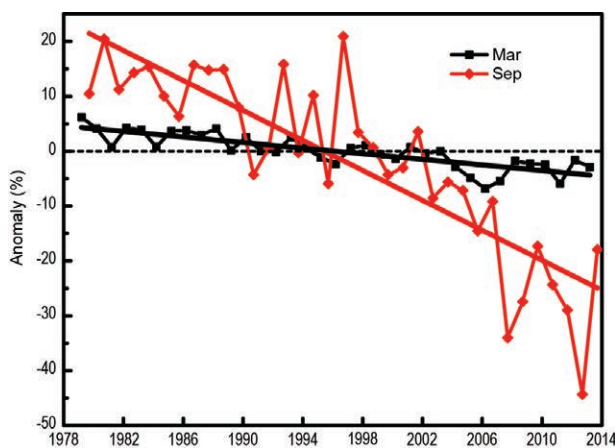
km² on 13 September 2013. This was 1.69 million km² higher than the record minimum of 3.41 million km² set in 2012 and the largest September minimum ice extent since 2006 (Fig. 5.13). However, the 2013 summer minimum extent was still 1.12 million km² (18%) below the 1981–2010 average minimum ice extent. The March 2013 ice extent reached a maximum value of 15.04 million km² (Fig. 5.13), 3% below the 1981–2010 average. This was slightly less than the March 2012 value, but typical of the past decade.

The September monthly average trend is –13.7% decade^{-1} relative to the 1981–2010 average (Fig. 5.13). Trends are smaller during March (–2.4% decade^{-1}) but are still decreasing and statistically significant. There was a loss of 9.69 million km² of sea ice between the March and September extents. This is the smallest seasonal decline since 2006.
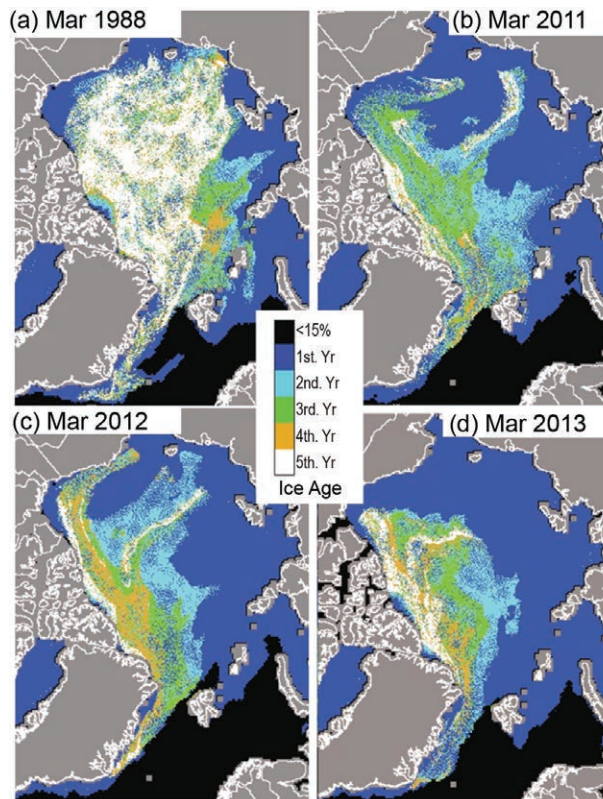
2) AGE OF THE ICE

Key ice physical properties, such as surface roughness, melt pond coverage, and thickness, vary according to the age of the ice. The age of the ice can be determined using satellite observations and drifting buoy records to track ice parcels over several years (Tschudi et al. 2010). This method has been used to provide a record of ice age since 1984. The distribution of ice of different ages (Fig. 5.14) illustrates the extensive loss in recent years of the older ice types (Maslanik et al. 2011).

Although the minimum sea ice extent increased somewhat in 2013 compared to recent years, the distribution of ice age continued to favor first-year ice (ice that has not survived a melt season), which

FIG. 5.14. Sea ice age in Mar (a) 1988, (b) 2011, (c) 2012, and (d) 2013, determined using satellite observations and drifting buoy records to track the movement of ice floes.

FIG. 5.13. Time series of ice extent anomalies measured in Mar (maximum ice extent) and Sep (minimum ice extent). The anomaly value for each year is the difference (in %) in ice extent relative to the average values for the period 1981–2010. The black and red lines are least squares linear regression lines.

is the thinnest ice type (e.g., Maslanik et al. 2007). In March 1988, 58% of the ice pack was composed of first-year ice, an amount that increased to 78% in March 2013. Meanwhile, the trends continue for the recent loss of the oldest and thicker ice types, which accelerated starting in 2005 (Maslanik et al. 2011). For the month of March, the oldest ice (four years and older) decreased from 26% of the ice cover in 1988 to 19% in 2005 and to 7% in 2013.

At the end of winter 2012/13, little multiyear ice was detected in much of the Beaufort Sea (Fig. 5.14d; Richter-Menge and Farrell 2013). There is no precedent in the satellite-derived record of ice age for the near-absence of old ice in this region. This condition appears to have been due to a combination of the previous year's record sea ice retreat and a lack of subsequent transport of multiyear ice into the Beaufort Sea during winter 2012/13. Negligible multiyear ice transport into the Beaufort Sea continued during summer 2013, consistent with stronger cyclonic (counterclockwise) wind forcing during this period (see section 5g). Multiyear ice did not drift into Siberian Arctic waters either, which is also rare. Instead,

multiyear ice remained confined to the region north of Greenland and northernmost Canada during 2013.

3) Ice thickness

Another key state variable for the Arctic sea ice cover is ice thickness. In recent years, ice thickness has been estimated over limited regions by aircraft, e.g., the NASA Operation IceBridge (Richter-Menge and Farrell 2013), and over large regions by satellite. The CryoSat-2 satellite, operated since 2011 by the European Space Agency, measures ice freeboard, the height of ice floes above the water line. Preliminary analysis indicates that the CryoSat-2 freeboard estimates are comparable to in situ field measurements, with a level of uncertainty that is comparable to other airborne and satellite-based observations (Ricker et al. 2014). Calculation of the actual sea-ice thickness from freeboard requires knowledge of snow depth, but in general higher freeboard indicates thicker sea ice. Therefore, freeboard maps in spring for the period 2011–13 are a proxy for sea ice thickness at the time of maximum ice extent. During the three years of CryoSat-2 observations, the average freeboard within the Arctic Basin decreased by 0.04 m, from 0.23 m in 2011 to 0.19 m in 2013 (Laxon et al. 2013). Assuming there were no significant changes in snow depth, the decline in freeboard amounts to an average sea ice thinning of 0.32 m, from 2.26 m in 2011 to 1.94 m in 2013. As with the ice age maps (Fig. 5.14), CryoSat-2 freeboard maps (Perovich et al. 2013, figure 22) indicate that most of the thickest and oldest ice occurs to the north of Greenland and northernmost Canada, and is a small proportion of the total sea ice cover at the end of winter.

g. Ocean temperature and salinity—M.-L. Timmermans, I. Ashik, I. Frolov, H. K. Ha, R. Ingvaldsen, T. Kikuchi, T. W. Kim, R. Krishfield, H. Loeng, S. Nishino, R. Pickart, I. Polyakov, B. Rabe, U. Schauer, P. Schlosser, W. M. Smethie, V. Sokolov, M. Steele, J. Toole, W. Williams, R. Woodgate, and S. Zimmerman

1) Summer sea surface temperature

Recent summers with reduced sea-ice cover (see section 5f) have seen increased solar absorption into the surface Arctic Ocean, with the distribution of sea surface temperatures (SST) reflecting sea ice retreat patterns. Arctic Ocean average SSTs in August 2013 ranged between ~0° and 4°C, with even higher SSTs in some marginal seas (Fig. 5.15). While most Arctic boundary regions displayed anomalously warm SSTs in August 2013, relative to the 1982–2006 August average (Fig. 5.15), cold anomalies were evident in the Chukchi and East Siberian Seas. The cooler SSTs
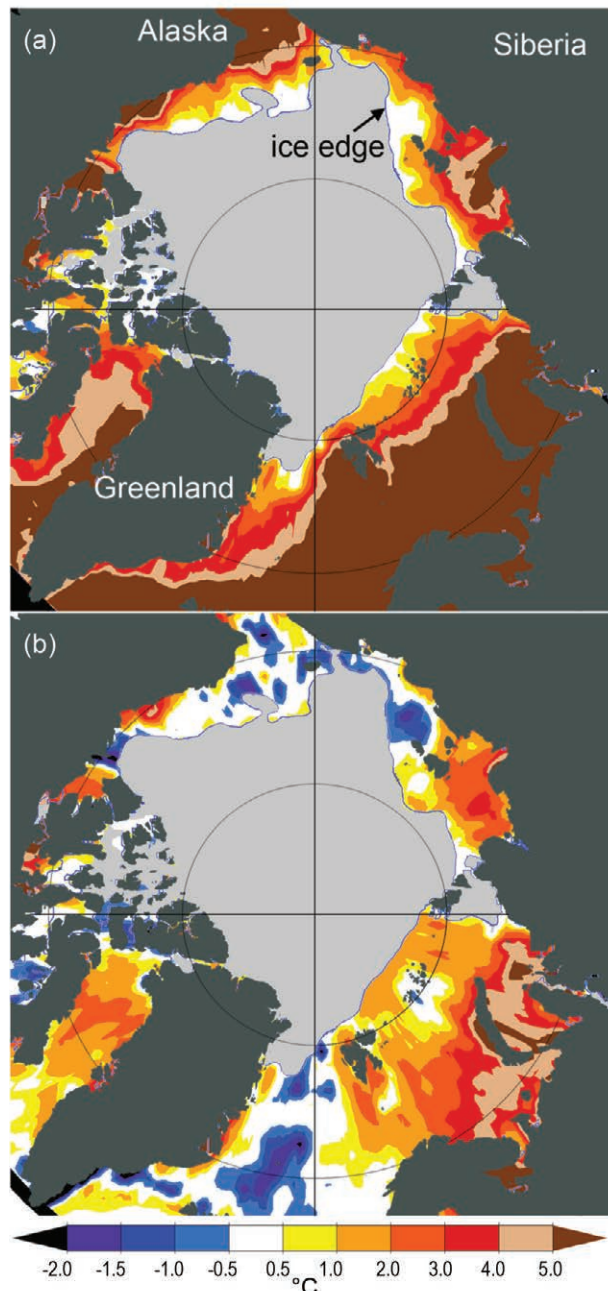
Fig. 5.15. (a) Average Aug 2013 SST (°C) and (b) Aug 2013 SST anomalies (°C) relative to the Aug 1982–2006 average. Anomalies are derived from satellite data according to Reynolds et al. (2007). The gray area shows the average Aug 2013 sea-ice extent according to the National Snow and Ice Data Center.

in these regions are linked to later and less extensive sea-ice retreat; anomalously cold August SSTs related to unusual sea-ice extent patterns were also observed in this region in 2012 (Timmermans et al. 2013b). Anomalously warm August SSTs in the Barents and Kara Seas are related to earlier ice retreat in these regions and possibly also to the advection of anomalously warm water from the North Atlantic.

Hydrographic data show surface waters in the vicinity of the Barents Sea Opening in September 2013 were about 3°C warmer than in September 2012. SSTs in the southern Barents Sea in September 2013 were as high as 11°C and up to 5°C above the 1977–2006 average (Trofimov and Ingvaldsen 2014).

2) UPPER OCEAN SALINITY

Salinity in the upper several hundred meters of the Arctic Ocean is set by sea ice melt/growth cycles, influxes from the Pacific and Atlantic oceans, river input, net precipitation, and redistribution by wind forcing and mixing. The central Canada Basin is the freshest region of the Arctic Ocean, and the saltiest upper ocean is observed at the boundaries of the Eurasian Basin and the Barents Sea (Fig. 5.16, which illustrates salinity at a depth of 20 m, within the well-mixed surface layer for most of the year). Relative to the 1970s, the major upper-ocean salinity differences in 2013 (similar to 2012; see Timmermans et al. 2013a, figure 24) were saltier waters in the central Eurasian Basin and fresher waters in the Beaufort Gyre region of the Canada Basin. The main differences in upper-ocean salinity in 2013 relative to 2012 included saltier surface waters in the region north of Greenland and Ellesmere Island, Canada, and in the northern part of the East Siberian Sea/western Canada Basin.
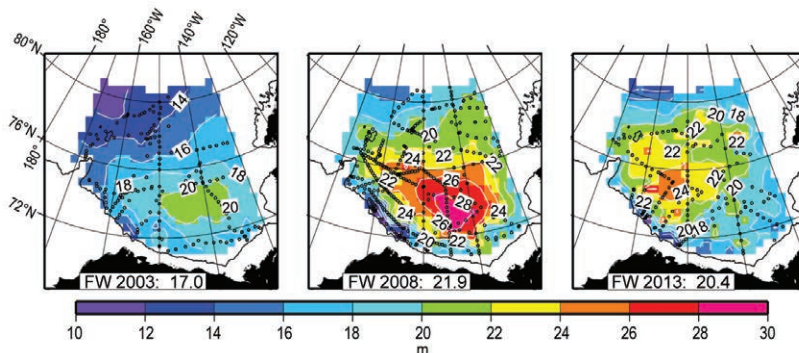
3) FRESHWATER CONTENT

Freshwater content in the Arctic Ocean has an important relationship to sea ice and climate; increased freshwater, for example, strengthens ocean stratification, impeding vertical heat transport from deeper waters. Liquid freshwater content in the upper Arctic Ocean basins showed an increasing trend from 1992 to 2012 of about 600 ±300 km³ yr⁻¹, based on observed salinity profiles (Rabe et al. 2014). The maximum liquid freshwater content anomaly is centered in the Beaufort Gyre (Fig. 5.17). In total, during 2003–13 the Beaufort Gyre accumulated more than 5000 km³ of freshwater (measured relative to a salinity of 34.8), a gain of approximately 25% (update to Proshutinsky et al. 2009) compared to the 1970s (see figure 5.24b in Timmermans et al. 2013b). Most of this increase occurred between 2004 and 2008.
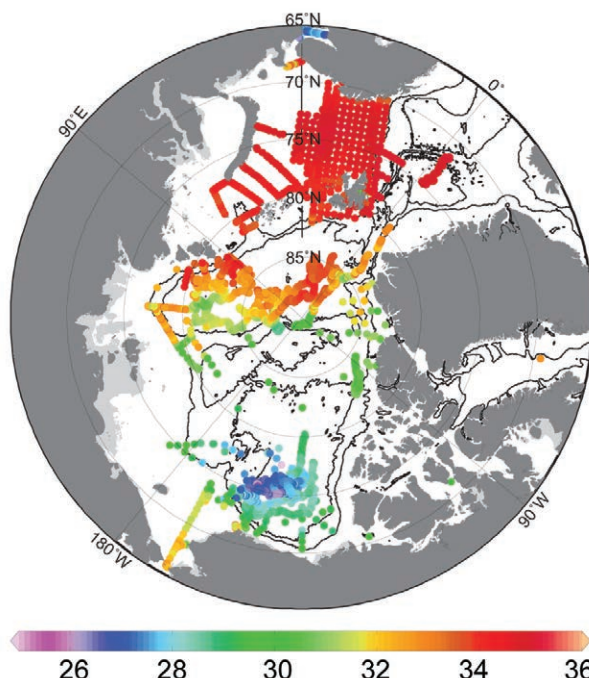
FIG. 5.16. Average salinity at 20-m depth in 2013. Contour lines show the 500-m and 2500-m isobaths. Salinities are reported using the Practical Salinity Scale (unitless). Data are from multiple sources, including various hydrographic expeditions by different countries and institutions, and ice-tethered profilers (http://www.whoi.edu/itp).

In 2013, a reduction in freshwater content by about 7% was observed relative to 2012 (*cf.* Timmermans et al. 2013b, figure 5.24c). This reduction may be attributed in part to stronger cyclonic (counterclockwise) wind forcing in summer 2013 (compared to previous years) that drove divergence of surface waters in the region. It is of note that trends in Beaufort Gyre heat


FIG. 5.17. Freshwater content (m, calculated relative to a reference salinity of 34.8) in the Beaufort Gyre of the Canada Basin based on hydrographic surveys in 2003, 2008, and 2013. Inset numbers at the bottom of each panel give total freshwater volume (×1000 km³) in the region. Black dots depict hydrographic station locations. Data are from the Beaufort Gyre Observing System (BGOS)/Joint Ocean Ice Studies (JOIS) project (http://www.whoi.edu/beaufortgyre) and other Canada Basin expeditions.

In recent years, ocean acidification has emerged as one of the dominant issues in marine science, particularly in high-latitude regions, where its progression has been greater than many other ocean basins (e.g., Fabry et al. 2009; Steinacher et. al. 2009; Mathis et al. 2011; Yamamoto-Kawai et al. 2013). It has been widely shown that the uptake of anthropogenic CO_2 from the atmosphere fundamentally alters the chemistry of seawater by lowering its pH (reducing the alkalinity) and decreasing the saturation states (Ω) of calcium carbonate ($CaCO_2$) minerals that are critical for the formation and maintenance of biogenic shells and tests (e.g., Feely et al. 2009; Cooley and Doney 2009; Kroeker et al. 2010).

Ocean acidification studies began in earnest in the Arctic Ocean during the early 1990s (Jutterström and Anderson 2005) and progressed slowly until a few large-scale studies of the Chukchi and Beaufort Seas (Fig. SB5.5), and the Nordic Seas were conducted in the 2000s. While these early studies were designed to broadly examine the carbon cycle, they provided the first evidence that aragonite became undersaturated in the bottom waters of the shallow shelf seas, particularly in summer and fall months (e.g., Bates et al. 2009), and that the halocline of the Canada Basin (Fig. SB5.5) was undersaturated in the carbonate mineral aragonite throughout the year (Jutterström and Anderson 2005). Since 2008, dozens of comprehensive ocean acidification projects have been conducted in the Arctic by a number of nations, including the United States, Canada, Sweden, Japan, South Korea, China, and Germany, with a commensurate increase in understanding of the controls on ocean acidification. New insights from surveys throughout the Arctic Ocean basin have clearly shown that the intrusion of anthropogenic CO_2 is not the only driver of reductions in pH and Ω in the region. Several other processes, such as melting sea ice, terrestrial and marine organic matter respiration, and upwelling are exacerbating the effects of ocean acidification, leading to rapid changes in the marine environment. Furthermore, the role that the differing shelf environments (inflow, interior, and outflow) have in conditioning the water column (Carmack and Wassmann 2006) throughout the year can be critical in determining the intensity of carbonate mineral undersaturation events on seasonal timescales. In a seminal paper on the changing carbonate chemistry of the Arctic Ocean, Yamamoto-Kawai et al. (2009) showed that increasing sea ice melt water in the Canada Basin is causing a sharp reduction in Ω in the surface waters due to the dilution effect on calcium carbonate ions. These results showed that, in summer, aragonite Ω had decreased from ~1.5 in 1997 to ~1.0 in 2008 and that the areas most affected were located in the eastern Canada Basin. If the
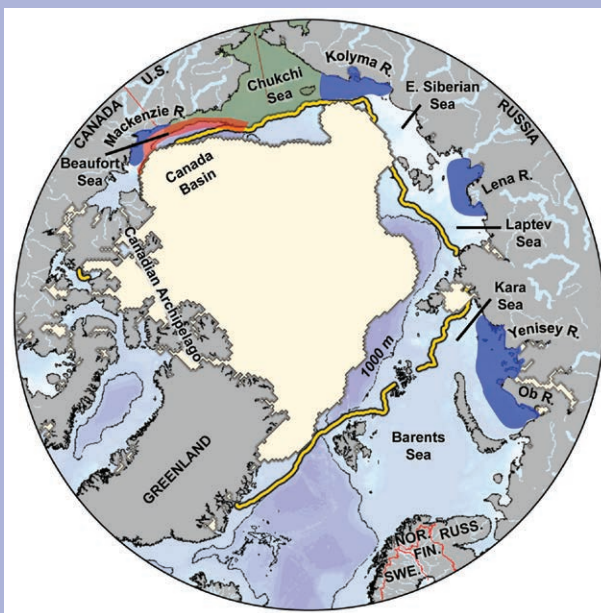
FIG. SB5.5. Polar view of the Arctic Ocean, highlighting the various regional drivers of ocean acidification: respiration-dominated shelves (green); plumes from the Ob, Yenisey, Lena, Kolyma, and Mackenzie Rivers (the major arctic rivers, blue); upwelling regions (red). Sep 2013 ice extent is light yellow and the mean Sep ice extent for 1976–present is the bold dark yellow line. Shelf types are: inflow shelves (Chukchi and Barents Seas), interior shelves (Kara, Laptev, East Siberian, and Beaufort Seas), outflow shelves (Canadian Arctic Archipelago). The shelf break is indicated by the 1000-m isobath (thin black line). Water with a depth >1000-m is purple.

current trajectory of sea ice loss continues (see section 5f), it is likely that larger areas of the Canada Basin will be inundated with waters that are undersaturated in aragonite, making them potentially corrosive to shell building organisms like pteropods (Bednaršek et al. 2012).

One of the most dominant drivers of carbonate mineral undersaturations over the Arctic continental shelves is the respiration of organic matter (Bates and Mathis 2009; Anderson et al. 2010) that is either produced during seasonally intense phytoplankton blooms or delivered by rivers and coastal erosion (Fig. SB5.5). In the Chukchi Sea (Fig. SB5.5), seasonally high rates of primary production are largely uncoupled from grazing and this leads to large quantities of organic matter to be exported to the bottom waters. As the organic matter is respired and converted back into CO_2, the pH and Ω of the bottom waters are reduced and aragonite as well as calcite can

become undersaturated for a few months each year (Mathis and Questel 2013). A portion of this water then ventilates the halocline of the Canada Basin (Mathis et al. 2007) and causes this subsurface layer at 75–150 m depth to be undersaturated in aragonite. The Chukchi Sea, like the Barents Sea (Fig. SB5.5), is an inflow shelf and receives a consistent supply of nutrients from the North Pacific Ocean via the Bering Strait (see section 5g) that sustain a productive growing season. However, the greater depth of the Barents Sea shelf, together with higher grazing rates, limit the degree of focused deposition of organic matter and the occurrence and severity of undersaturation events in that region.

The interior shelves of the Arctic Ocean (Beaufort, Kara, Laptev, East Siberian; Fig. SB5.5) have much lower rates of primary production due to nutrient limitation; however, high rates of riverine and terrestrial inputs of organic matter sustain similarly intense respiration rates and lead to a lower Ω (Fig. SB5.5). Broad areas of undersaturation have been observed over the Eurasian shelves due to this process (e.g., Anderson et al. 2010). It is likely that both primary production and terrestrial inputs of organic matter will increase in the coming decades as warming in the region continues (Lavoie et al. 2010; Arrigo and van Dijken 2011), which could lead to increased respiration and further reductions in Ω. The Canadian Arctic Archipelago (Fig. SB5.5), an outflow shelf downstream from the Beaufort Sea, is already experiencing aragonite undersaturations for several months each year due to the impacts of ice melt, respiration, and upwelling (Shadwick et al. 2011; Yamamoto-Kawai et al. 2013).

Finally, the upwelling of water that is undersaturated in aragonite from the halocline of the Arctic Ocean (Mathis et al. 2012) can also expose shelf regions to conditions that could be corrosive to calcifying organisms (Fig. SB5.5). The upwelling of high CO_2, low Ω water can occur at any time during the year, but will likely increase in frequency as sea ice continues to decline, and particularly in fall months when storm conditions are at their peak (Pickart et al. 2011, 2013).

Through continuing observations and synthesis activities, it is becoming more apparent that the Arctic Ocean is on a dangerous ocean acidification trajectory that could lead to direct impacts on calcifying organisms, many of which are keystone species such as clams and pteropods. The Arctic is facing multiple drivers for enhanced ocean acidification. The loss of sea ice in summer is allowing more CO_2 to be taken up directly from the atmosphere as the ice melt reduces the buffer capacity of the waters and the continental shelves are being exposed to waters that are undersaturated in carbonate minerals due to organic matter respiration and upwelling. At a time when the Arctic Ocean and adjacent lands are undergoing rapid change, it will be critical to maintain observations of the extent of ocean acidification in this basin.

content (calculated relative to freezing temperature in the upper 1000 m) generally follow freshwater trends; there is ~25% more heat on average in the summer now compared to the 1970s.

4) Pacific Water layer

The Pacific Water layer in the Arctic Ocean originates from the Bering Strait inflow and resides in the Canada Basin at depths between about 50 and 150 m. Pacific Water is a major source of heat, freshwater, and nutrients to the Arctic Ocean. As reported in Woodgate et al. (2012), 2011 was a high transport year for Pacific Water inflow through the Bering Strait, with transports being ~1.1 Sv, much higher than the accepted climatology (1991–2003) of ~0.8 Sv (Woodgate et al. 2005). In contrast, annual average transport in 2012 (the most recent year for which data are available) was close to average. The annual average temperature of the Pacific Water layer in 2012 was colder than the last decade and comparable to the annual averages of the 1991–2001 period. These two factors yield a heat flux in 2012 comparable to the record low in 2001. Freshwater transport was also reduced in 2012 compared to 2011.

Pacific Water enters the Canada Basin via different mechanisms and pathways. Moored measurements of the Pacific water boundary current in the Beaufort Sea north of Alaska (the Beaufort shelfbreak jet) show an 80% decrease in volume transport in the current between 2002 and 2011 (Brugler et al. 2014), where this decrease is predominantly in the summer months. Brugler et al. (2014) attribute the decrease in transport to an increase in easterly winds and propose that in recent years Pacific heat and freshwater are being advected directly north into the Canada Basin interior instead of progressing eastward in the Beaufort shelfbreak jet.

In the central Canada Basin, observations show heat and freshwater content in the Pacific Water layer increased by about 40% during 2003–13, with the

largest increases in the southern Canada Basin before 2010. Freshwater content has been relatively stable since 2010. In 2013, maximum Pacific Water layer temperatures over the abyssal plain of the Canada Basin were ~0.5°C.

5) Atlantic Water layer

Warm water of North Atlantic origin, lying below the halocline at depths between about 200 and 900 m (but nearer the surface in the vicinity of the Barents Sea Opening and Fram Strait), is characterized by a warm core with temperatures >0°C and salinities >34.5. The transport of ocean heat in the Atlantic Water layer potentially contributes to the surface ocean heat budget and affects the sea ice volume. Atlantic Water temperatures are generally around 1°–2°C higher in the Eurasian Basin than in the Canadian Basin (see figure 5.22b in Proshutinsky et al. 2012). In 2013, the warmest Atlantic Water temperatures (~5°C) were observed in the Barents Sea. The coolest temperatures (~0°C) were observed off the north coast of Greenland. No significant changes were observed in 2013 in the Atlantic Water layer compared to 2012 conditions. Maximum temperatures of the Atlantic Water flowing into the southern Barents Sea in 2013 were about 0.5°C higher than the 1977–2006 average (Trofimov and Ingvaldsen 2014). Relative to 1970s conditions, Atlantic Water temperature anomalies were ~0.5°–1°C warmer in the Eurasian Basin and <0.5°C warmer in the Canadian Basin. There was little to no temperature anomaly (<0.1°C) at the southeast boundary of the Canada Basin nor in the basin boundary regions adjacent to Greenland and the Canadian Archipelago.

h. *Terrestrial snow cover*—C. Derksen, R. Brown, and K. Luojus
1) Snow cover extent

Northern Hemisphere spring snow cover extent (SCE) anomalies (relative to a 1981–2010 reference period) were computed from the weekly NOAA snow chart Climate Data Record [CDR; maintained at Rutgers University and described in Estilow et al. (2013)] for months when snow cover is confined largely to the Arctic. SCE showed a continued reduction from the historical mean during May and June 2013 (Fig. 5.18a). For Eurasia, a new record low May SCE was established (27% below average), and June SCE tied for the second lowest since 1967. Across North America, April SCE was well above average (16% above the 1981–2010 mean), May SCE was near average, and June SCE well below average (34% below the 1981–2010 mean). The contrasting SCE anomalies

between North America and Eurasia during May 2013 were consistent with continental differences in spring air temperature anomalies (warm over the Eurasian Arctic; cold over North American Arctic; see Fig. 5.2b).

The shift to increasingly negative SCE anomalies as the melt season progressed is consistent with observed trends over the past decade (Fig. 5.18a; Derksen and Brown 2012). The rate of snow cover loss over Northern Hemisphere land areas in June between 1979 and 2013 was −19.9% decade[-1] (relative to the 1981–2010 average; updated from Derksen and Brown 2012). The rate of loss in the June SCE exceeds the rate of September sea ice loss over the same time period (−13.7% decade[-1]), adding further compelling evidence of the observed rapid response of both the terrestrial and marine cryosphere to Arctic amplification in surface temperature trends. The rate of reduction in Arctic June SCE over the period of the NOAA data record continues to exceed the CMIP5 (Coupled Model Intercomparison Project Phase 5) model ensemble simulated and projected (historical + scenario rcp8.5) rate of decrease (Derksen and Brown 2012)

2) Snow cover duration

The timing of snow cover onset in fall is influenced by both temperature and precipitation. Snow cover duration (SCD) departures derived from the NOAA daily IMS snow cover product (Helfrich et al. 2007) identified earlier-than-normal snow cover onset over Scandinavia (Fig. 5.18b), with no notable departures over other Arctic regions (earlier-than-normal snow onset was observed for a midlatitude region of North America and southeastern Eurasia; see section 2c2 for more detail). The negative SCE anomalies for May and June (Fig. 5.18a) are reflected in earlier-than-normal snow melt across the Canadian tundra and eastern Siberia (Fig. 5.18c). Snow cover persisted longer than normal across northwestern Europe, which drove the positive Eurasian SCE anomalies for April. This region was snow free by May, so the longer-than-normal spring SCD departures in this region in April had no impact on the record setting low SCE across Eurasia in May.

3) Snow depth

April snow depth anomalies from the Canadian Meteorological Centre daily gridded global snow depth analysis (Brasnett 1999; Fig. 5.18d) were positive over most of Eurasia (average anomaly of +16.9% relative to 1999–2010 average) and North America
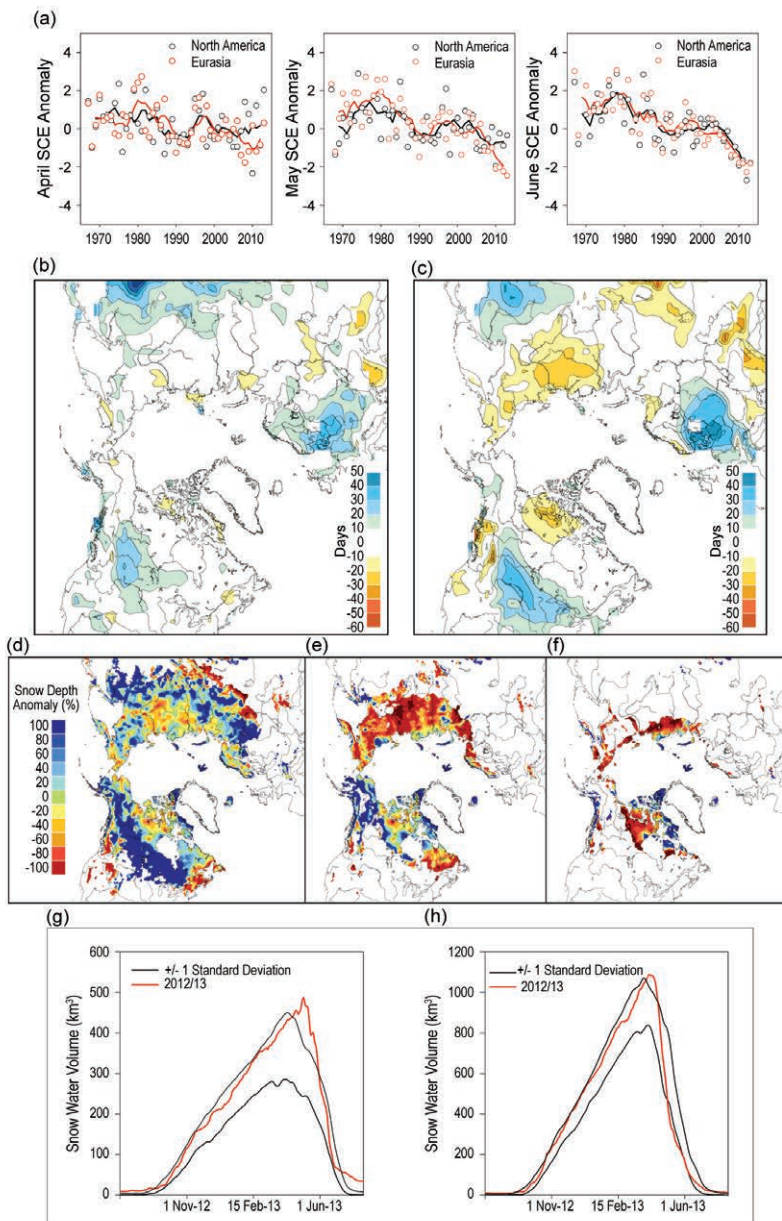
FIG. 5.18. (a) Monthly Arctic snow cover extent standardized (unitless) anomaly time series (with respect to 1988–2007) from the NOAA snow chart CDR for Apr, May, and Jun 1967–2013 (solid lines denote 5-yr moving average). Snow cover duration departures (with respect to 1998–2010) from the NOAA IMS (Interactive Multisensor Snow and Ice Mapping System) data record for the (b) 2012 fall season and (c) 2013 spring season. Snow depth anomaly (% of 1999–2010 average) from the Canadian Meteorological Centre (CMC) snow depth analysis for (d) Apr, (e) May, and (f) Jun 2013. Daily 2012/13 time series (red) of Arctic snow water volume for (g) North America and (h) Eurasia derived from the CMC snow depth analysis. The solid black lines show the ±1 std. dev. range about the mean SWE over 1998/99 to 2011/12 snow seasons. Note different y-axis ranges.

(average anomaly of +29.4%). This is consistent with the negative winter season Arctic Oscillation (DJF average of −1.12; weaker Arctic jet favorable to cold air outbreaks), which produced below-average winter season temperatures over subarctic Eurasia and North America (see Fig. 5.2a). By May, however, the Eurasian snow depth anomalies were strongly negative (Fig. 5.18e; average anomaly of −52.1%), illustrating the rapid response of snow conditions to positive surface temperature anomalies over most of Eurasia (see Fig. 5.2) concurrent with below-normal cloud cover (as estimated by the ERA-Interim reanalysis; not shown).

4) Snow water equivalent

The quick transition from above-normal to below-normal snow depth was also captured by the daily time series of Arctic snow water equivalent (SWE; land areas north of 60°N) derived from the Canadian Meteorological Centre analysis (Fig. 5.18g,h). Before melt onset, the total SWE was above the average for the data record (since 1998) over both Eurasia and North America. During a two-week period in mid-May, the record high SWE over Eurasia plummeted to well below average (Fig. 5.18h). The decline in SWE was less dramatic for North America because regionally extensive positive temperature anomalies (also concurrent with below-average cloud cover and above-average surface net radiation, see Figs. 5.5b, 5.6b) did not set in until June. As in 2012, rapid snowmelt (not anomalously low winter season snow accumulation) was the main process responsible for the record-setting loss of Eurasian spring snow cover in May 2013 and the below-normal June 2013 SCE in North America.

i. *Glaciers and ice caps (outside Greenland)*—M. Sharp,
G. Wolken, M-L. Geai, D. Burgess, A. Arendt, B. Wouters, J. Kohler,
L. M Andreassen, and M. Pelto

Mountain glaciers and ice caps cover an area of over 400 000 km² in the Arctic and have been a major contributor to global sea level change in recent years (Gardner et al. 2011; Jacob et al. 2012). They gain mass by snow accumulation and lose mass by surface melt and runoff and by iceberg calving where they terminate in water (ocean or lake). The climatic mass balance (B_{clim}, the difference between annual snow accumulation and annual runoff) is a widely used index of how glaciers respond to climate variability and change. Snow accumulation minus mass losses by iceberg calving and runoff gives the total mass balance (ΔM).

Since many B_{clim} measurements for the 2012/13 mass balance year are not yet available, we begin by summarizing measurements from 24 Arctic glaciers in 2011/12 (World Glacier Monitoring Service 2014). These glaciers are located in Alaska (three), Arctic Canada (four), Iceland (six), Svalbard (four), Norway (two), and Sweden (five) (Fig. 5.19; Table 5.2). For the monitored Arctic glaciers as a whole, B_{clim} in 2011/12 was negative (Fig. 5.20), although 2011/12 was the eighth least negative year since 1989.

All but seven of the glaciers (Wolverine and Lemon Creek in coastal southern Alaska, Kongsvegen in Svalbard, Engabreen in northern Norway, and Rabotsglaciären, Storglaciären, and Tarfalaglaciären in northern Sweden) had a negative B_{clim}, i.e., loss of ice mass. For the four Scandinavian glaciers with
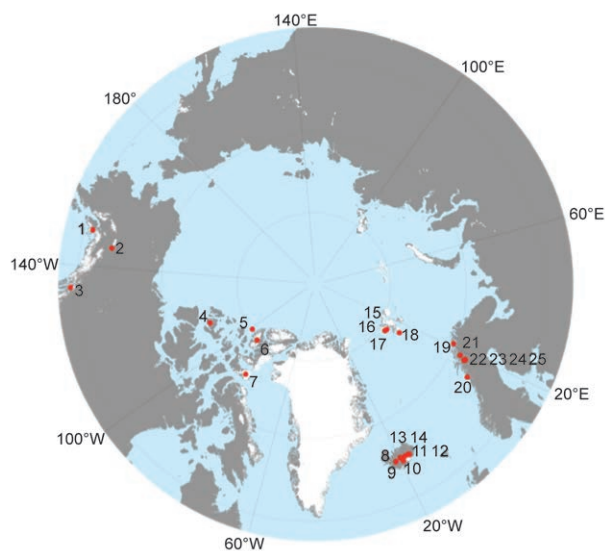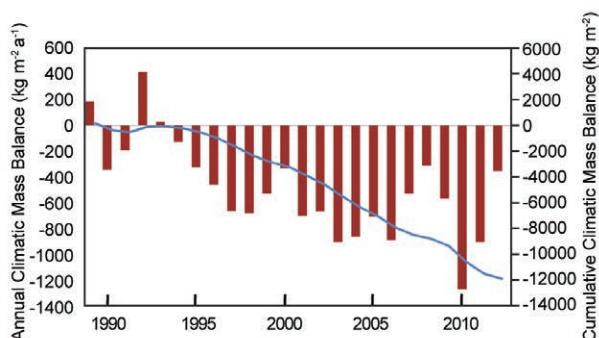
FIG. 5.20. Average annual (red bars) and cumulative (blue line) climatic mass balance (B_{clim}) of 24 Arctic glaciers (see Fig. 5.19) monitored during the period 1988/89–2011/12.

positive B_{clim} in 2011/12, the recorded values were among the 5–7 most positive in the period of record for each glacier. This is most likely a result of anomalously cool temperatures over the region in summer 2012 (see Figs. 5.2c, 5.4a). In the Canadian Arctic, however, the 2011/12 climatic balances were each among the four most negative in their 50–52-year records, extending the unusually high mass loss rates from that region since 2006/07 (Sharp et al. 2011). This is consistent with the extensive surface melting and mass loss recorded in Greenland in summer 2012, which was a result of advection of warm southerly air masses (Tedesco et al. 2013a). B_{clim} was negative in interior Alaska (Gulkana Glacier) and positive in coastal southern Alaska (Wolverine and Lemon Creek glaciers), where winter snowfall was unusually high. In coastal southern Alaska, the 2011/12 balances were among the 5–10 most positive ever recorded at the glaciers sampled. The mass balance of Hansbreen in southern Spitsbergen, Svalbard, was the second most negative in the 24-year record.

Trends of increasingly negative cumulative balances are evident in regional total mass balance estimates (ΔM) for Arctic Canada and Alaska derived using GRACE satellite gravimetry (Fig. 5.21). However, GRACE estimates of ΔM for the 2012/13 mass balance year are incomplete at the time of writing. Nevertheless, available measurements of ΔM for all the glaciers and ice caps in the Canadian Arctic Archipelago (CAA) suggest that the region gained mass between the ends of the summer 2012 and 2013 melt seasons, while mass accumulation in the Gulf of Alaska region over winter 2012/13 was significantly less than in winter 2011/12 (Fig. 5.21). It is not yet possible, however, to determine the sign of the mass balance in the Gulf of Alaska region in 2012/13 be-


FIG. 5.19. Locations of 25 Arctic glaciers with long-term records of annual climatic mass balance (B_{clim}). See Table 5.2 for glacier names.

Table 5.2. Measured annual climatic mass balance (B_{clim}) of 24 glaciers in Alaska, the Canadian Arctic, Iceland, Svalbard, and northern Scandinavia for 2009/10, 2010/11, and 2011/12 (data from the World Glacier Monitoring Service). Additional 2012/13 data for glaciers in Svalbard and Norway were provided by J. Kohler and L. Andreassen. Numbers in the far left column identify glacier locations in Fig. 5.19.

Region	Glacier (Length of record in years)	Climatic Balance (kg m^{-2} yr^{-1})			
		2009/10	2010/11	2011/12	2012/13
Alaska					
1	Wolverine (47)	-85	-1070	510	
3	Lemon Creek (60)	-580	-720	450	
2	Gulkana (47)	-1832	-1290	-790	
Arctic Canada					
7	Devon Ice Cap (52)	-417	-683	-503	
5	Meighen Ice Cap (51)	-387	-1310	-1118	
4	Melville S. Ice Cap (50)	-939	-1339	-1556	
6	White (50)	-188	-983	-951	
Iceland					
8	Langjökull S. Dome (16)	-3800	-1279	-542	
9	Hofsjökull E	-2830			
9	Hofsjökull N	-2400			
9	Hofsjökull SW	-3490			
14	Köldukvislarjökull (20)	-2870	-754	-289	
10	Tungnaarjökull (21)	-3551	-1380	-1294	
13	Dyngjujökull (15)	-1540	+377	-975	
12	Brúarjökull (20)	-1570	+515	-759	
11	Eyjabakkajökull (21)	-1750	+525	-954	
Svalbard					
17	Midre Lovenbreen (45)	-200	-920	-260	-940
16	Austre Broggerbreen (46)	-390	-1010	-180	-1090
15	Kongsvegen (26)	+130	-440	210	-610
18	Hansbreen (24)	-14	-280	-150	
Norway					
20	Engabreen (43)	-520	-910	1140	-1780
19	LangfjordjØkulen (22)	-760	-1257	-760	-2610
Sweden					
21	Marmaglaciaren (23)	-500	-1450	-90	
22	Rabots Glaciar (31)	-1080	-2110	20	
23	Riukojietna (26)	-960	-1080	-90	
24	Storglaciaren (67)	-690	-1060	680	
25	Tarfalaglaciaren (18)	-1060	-1820	830	

cause the glaciers were still losing mass at the end of the available GRACE record.

In summer 2013, near-surface summer air temperatures over Greenland and Arctic Canada were up to 3.5°C cooler than in the period 2007–12 (see section 5j, Figs. 5.2c, 5.4a). The relatively low mass loss measured in summer 2013 by GRACE in Arctic Canada (Fig. 5.21), and the lower melt extent and less negative surface mass balance on the Greenland ice sheet compared to 2012 (see section 5j), are consistent with the air temperature observations for these cold, dry regions, where variability in average summer temperature accounts for much of the interannual variability in B_{clim}. This contrasts with more maritime regions, e.g., Iceland and the mountains adjacent to the Gulf of Alaska, where variability in winter precipitation is also a factor.

By contrast, summer 2013 was very warm over some glaciated regions of the Arctic, including southern Alaska, Novaya Zemlya, Svalbard, northern Scandinavia, and eastern Iceland (see Figs. 5.2c, 5.4a). In northwest Svalbard and northern Norway, this warm summer followed a winter with unusually low snowfall. For northwest Svalbard, this resulted
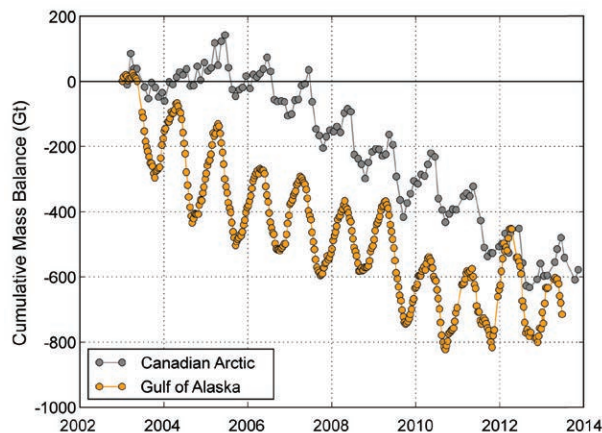
Fig. 5.21. Cumulative total mass balance (Gt) of glaciers in the Canadian Arctic and the Gulf of Alaska region for the period 2003–13. Note that available measurements for the Gulf of Alaska do not cover the full 2012/13 mass balance year. The total uncertainty from 2003 to 2010 in the Gulf of Alaska and Canadian Arctic mass trends was ±11 Gt yr^{-1} (Luthcke et al. 2013) and ±7 Gt yr^{-1} (update of Gardner et al. 2013), respectively. Uncertainties in the GRACE time series result from different approaches used to process the raw Level 1B satellite observations, signal leakage in and out of the solution domain, and different methods for modeling non-glacier sources of mass variability.

in the second or third most negative annual climatic balances on record in 2012/13, while for northern Norway it resulted in the single and second most negative annual climatic balances (Table 5.1). In Alaska, final values for the annual climatic mass balance have not yet been determined, but measurements in late summer 2013 suggest that 2012/13 may have been the most negative balance year on record at coastal Wolverine Glacier and the fifth most negative at Gulkana Glacier in the Interior (preliminary data provided by the United States Geological Survey). In southeastern Alaska, both Lemon Creek and Taku Glaciers had above-average equilibrium line altitudes of 1050 and 1115 m, respectively, at the end of summer 2013, which suggests a moderately negative annual climatic balance (B_{clim}) in that region.

j. Greenland Ice Sheet—M. Tedesco, J. E. Box, J. Cappelen, X. Fettweis, T. S. Jensen, T. Mote, A. K. Rennermalm, L. C. Smith, R. S. W. van de Wal, and J. Wahr

1) SATELLITE OBSERVATIONS OF SURFACE MELTING AND ALBEDO

Melt estimates over the Greenland Ice Sheet obtained from passive microwave data (Mote and Anderson 1995; Mote 2007) indicate that melting during summer (June–August, JJA) 2013 was near the long-term average for the period 1981–2010. On 26 July, melt area reached a maximum, covering 44.1% of the ice sheet surface. This was much smaller than the record of 97% set in 2012 (Nghiem et al. 2012; Tedesco et al. 2013b,c) and ranked 14th in the 35-year period of record (1979–2013). Moreover, the average melt area (the melting area averaged over the entire summer of 2013) of 16.7%, ranked 16th in the period of record and was the lowest annual value since 2000. For comparison, the average melt area during the record-setting summer of 2012 was 33.5%. The frequency of melting was slightly above the 1981–2010 average along the western and northwestern ice sheet margins, but lower than average in the south and southeast. In terms of number of melting days, surface melting during 2013 occurred for more than 100 days in some southwestern ice sheet margin areas, consistent with the long-term trend (Fig. 5.22a).

The average ice sheet-wide albedo derived from the Moderate-resolution Imaging Spectroradiometer (MODIS; e.g., Box et al. 2012) during summer 2013 was the highest (~0.72) since 2008, interrupting a period of increasingly negative and record albedo values since observations began (Fig. 5.23; Box et al. 2012; Tedesco et al. 2011, 2013b). Albedo for JJA 2013 was above the 2000–11 average along the southwest,
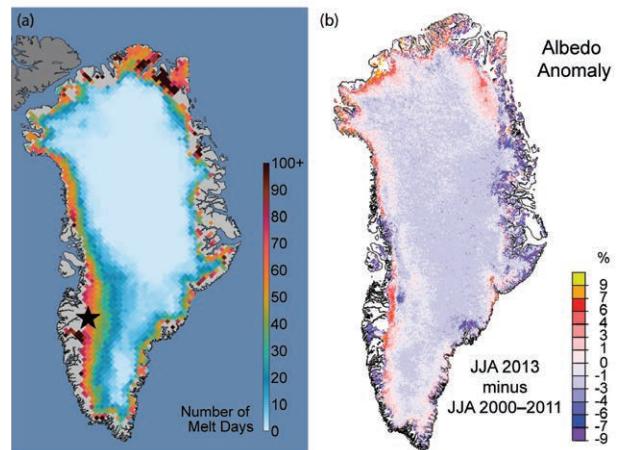

FIG. 5.22. (a) Cumulative number of melting days on the Greenland Ice Sheet between 1 Jan and 23 Sep 2013. (Source: National Snow and Ice Data Center) (b) Greenland Ice Sheet albedo anomalies in summer 2013 relative to the 2000–11 average derived from MODIS (Moderate-resolution Imaging Spectroradiometer). The black star on the west coast of Greenland in (a) marks the location of Kangerlussuaq and the K-transect to its east.

northwest, and northeast regions and coasts of the ice sheet and below average for the east and southeast regions (Fig. 5.22b; Tedesco et al. 2013a). Areas of low albedo are generally associated with areas with prolonged melting.

2) SURFACE MASS BALANCE AND RIVER DISCHARGE

Surface mass balance measurements made ~20 km east of Kangerlussuaq (Fig. 5.22a) between 340 and 1500 m above sea level (a.s.l.) along the 'K-transect' (van de Wal et al. 2005, 2012) indicate that melting along the transect in 2013 was below the 1990–2010 average, particularly near the ice margin (Fig. 5.24a).
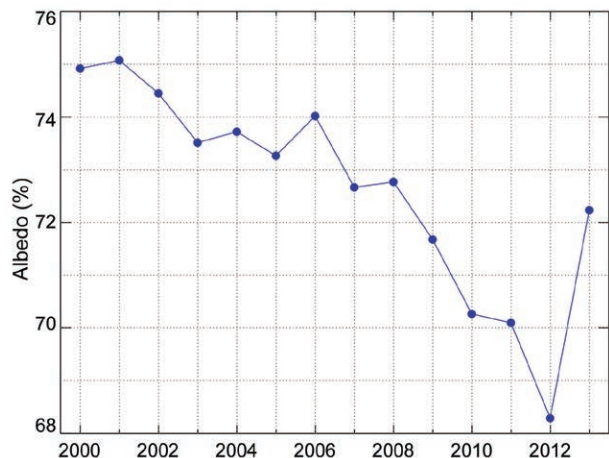
FIG. 5.23. Area-averaged albedo of the Greenland Ice Sheet in summer since 2000 derived from MODIS data.
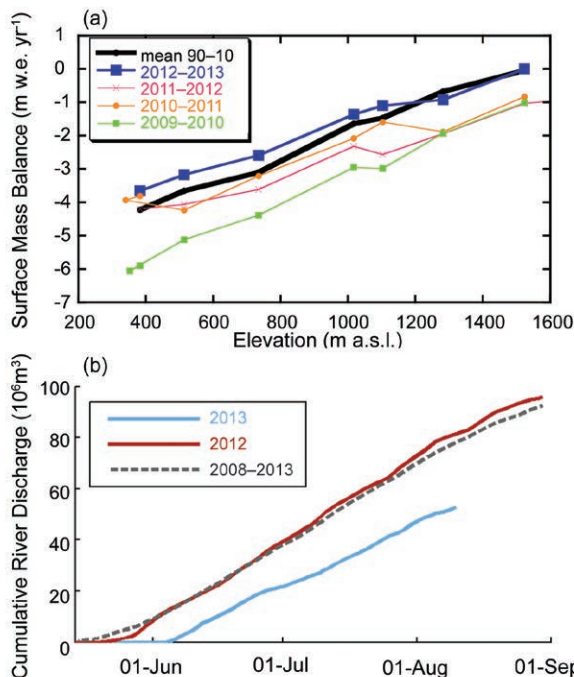
FIG. 5.24. (a) Surface mass balance (meters of water equivalent per year) as a function of elevation along the K-transect for four years since 2009/10, and the long-term average for 1990–2010. (b) Cumulative river discharge from the AK4 catchment (~20 km east of Kangerlussuaq) in southwest Greenland (see Fig. 5.22a) in 2013 compared with 2012 and the 2008–13 average.

The 2013 estimated equilibrium line altitude on the transect was near the long-term average position of 1500 m a.s.l., in strong contrast to its upslope migration to ~2700 m during the very warm summer of 2012 (e.g., Tedesco et al. 2013c).

Consistent with surface mass balance estimates, river discharge observations of a small basin of the Kangerlussuaq catchment, which includes much of the K-transect (Rennermalm et al. 2012, 2013a,b), reveal a later melt season onset in 2013 and lower flow conditions compared to previous years. Cumulative river discharge in 2013 (Fig. 5.24b) was the lowest recorded during the instrumental record beginning in 2008, confirming that meltwater runoff from the ice margin in this area of southwestern Greenland was below previous years (Tedesco et al. 2013a).

3) SURFACE AIR TEMPERATURE OBSERVATIONS

Near surface air temperature (NSAT) data recorded at long-term meteorological stations (Cappelen 2013; http://www.dmi.dk/fileadmin/Rapporter/TR/tr13-04.pdf) indicate that the outstanding surface temperature feature in 2013 was a consistent warm anomaly along the west Greenland coast during March (see Fig. 5.2a). A record warm March was recorded at Pituffik/Thule AFB, where the NSAT anomaly relative to 1981–2010 baseline was +7.7°C, the warmest on record since 1948. Similarly, the Upernavik and Kangerlussuaq March NSAT anomalies were +7.7° and +8.6°C, respectively. In contrast, during the summer months (June–August) NSAT values were generally near or below one standard deviation of anomalies relative to the 1981–2010 average, indicating that summer 2013 NSATs were normal with respect to that period. Wide-area air temperature anomalies are broadly consistent with the data for individual stations (Tedesco et al. 2013a).

In contrast to the previous six summers, characterized by negative North Atlantic Oscillation (NAO) phases, summer 2013 was characterized by persistent positive NAO phases, inducing lower-than-normal 500-hPa geopotential heights over Greenland. Consequently, warm, southerly air masses were diverted eastward from Greenland and northerly airflow in west Greenland (see Fig. 5.4b) promoted cooler, wetter, and cloudier weather than normal, and less melting than in recent years, as reported above.

4) SATELLITE OBSERVATIONS OF ICE MASS AND MARINE-TERMINATING GLACIERS

Based on GRACE satellite measurements, the cumulative ice sheet loss was 570 ±100 Gt between the end of April 2012 and the end of April 2013, which corresponds to the period between the beginning of the 2012 and 2013 melt seasons. The mass loss was more than twice the average annual loss rate of 260 ±100 Gt during 2003–12 (Fig. 5.25). The 2012/13 mass loss is the largest annual loss rate for Greenland in the GRACE record, mostly reflecting the large mass loss during the summer of 2012 (Tedesco et al. 2013c).

LANDSAT and ASTER images of 41 of the widest marine-terminating glaciers in summer 2013 indicate a net cumulative area change of −20 km² since summer 2012 (after Box and Decker 2011). This is the second smallest area change on record and 118 km² less than the average annual area change (−138 km²) since 2000. The largest local increases in area between 2012 and 2013 occurred at Petermann (+16 km²), Ryder (+4 km²), Nioghalvfjerdsbrae/79 (+3 km²) glaciers. The largest local area decreases occurred at Zachariae (−16 km²), Humboldt (−10 km²), and Helheim glaciers (−4 km²).
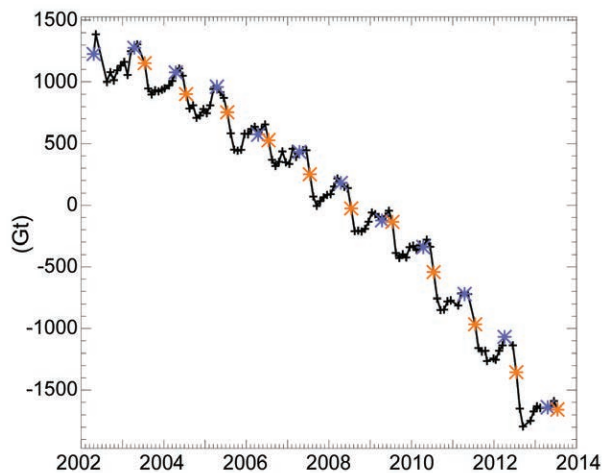
FIG. 5.25. Monthly changes in the total mass (Gt) of the Greenland Ice Sheet estimated from GRACE measurements since 2002. Blue and orange asterisks denote Apr and Jul values, respectively. Black asterisks denote all other months. Total ice mass change estimates from GRACE for summer 2013 are unavailable because the K-band ranging system was switched off during Aug and Sep to preserve battery life. The uncertainty in the mass loss estimate between Apr 2012 and Apr 2013, ±100 Gt yr⁻¹, is due to scatter in the data; estimates of leakage from imperfectly modeled signals external to the ice sheet; errors in the correction for glacial isostatic rebound; and uncertainty in the scaling factor used to correct for the limited horizontal resolution of GRACE. Velicogna and Wahr (2013) discuss uncertainties in GRACE estimates of polar ice sheet mass.

### k. *Lake ice*—C. R. Duguay, L. C. Brown, K.-K. Kang, and H. Kheyrollah Pour

Lake ice is a sensitive indicator of climate variability and change. Lake ice phenology, which includes freeze-up (ice-on) and break-up (ice-off) dates, and ice cover duration, are largely influenced by air temperature changes and are, therefore, robust indicators of regional climate conditions (Duguay et al. 2006; Kouraev et al. 2007). Long-term trends in ground-based observational records reveal increasingly later freeze-up and earlier break-up dates, closely corresponding to increasing air temperature trends, but with greater sensitivity at the more temperate latitudes (Brown and Duguay 2010; Prowse et al. 2011). Broad spatial patterns in these trends are also related to major atmospheric circulation patterns originating from the Pacific and Atlantic Oceans, e.g., the El Niño-La Niña/Southern Oscillation, the Pacific North American pattern, the Pacific decadal oscillation, and the North Atlantic Oscillation/Arctic Oscillation (Bonsal et al. 2006; Prowse et al. 2011).

Despite the robustness of lake ice as an indicator of climate change, a dramatic reduction in ground-based observations has occurred globally since the 1980s (Lenormand et al. 2002; Duguay et al. 2006; IGOS 2007; Jeffries et al. 2012). Consequently, satellite remote sensing has assumed a greater role in observing lake ice phenology (Latifovic and Pouliot 2007; Brown and Duguay 2012; Kropáček et al. 2013; Surdu et al. 2014).

Freeze-up (FU) in 2012/13 occurred earlier than the 2004–12 average by ~1–3 weeks for most regions of the Arctic (Fig. 5.26a). Notable exceptions include Lakes Ladoga and Onega (western Russia) and lakes of smaller size in southern Norway and adjacent areas of Sweden (~4–5 weeks earlier). Arctic-wide, few lakes experienced later FU than normal (~1–2 weeks later); they were clustered mainly throughout northern Quebec, the northwest Canadian Arctic, northern Finland, and the adjacent areas of Russia, with lakes in a small, localized region of southern Sweden experiencing notably later FU than normal (~2–5 weeks). This is in contrast to the 2011/12 ice season when FU occurred almost a full month later for most lakes located in the southern portion of northern Europe and part of the central portion of Arctic Canada (i.e., Great Slave Lake and Lake Athabasca regions; Duguay et al. 2013).

Break-up (BU) dates in 2013 occurred ~1–3 weeks earlier than the 2004–12 average over much of the Arctic, with the exception of Baffin and Ellesmere Islands in Canada (~1–4 weeks later), consistent with cooler-than-normal spring and summer temperatures in the high Canadian Arctic (see Figs. 5.2b,c), and the southern part of Scandinavia and western Russia (~1–5 weeks later; Fig. 5.26b). Lakes showing the largest BU anomalies with earlier dates (~3–4 weeks earlier) in 2013 are found in Siberia, consistent with spring-time positive air temperature anomalies and early snow cover loss (see sections 5b and 5h). Break-up was also particularly early (by ~2–3 weeks) in the western Hudson Bay and Victoria Island regions of Canada. Earlier BU anomalies of the same magnitude were reported throughout Siberia in 2012 (Duguay et al. 2013). In general, the spatial pattern of ice cover duration (ICD; Fig. 5.26c) anomalies followed closely that of BU anomalies. ICD for 2012/13 was shorter by ~1–4 weeks in regions adjacent to Hudson Bay, as well as in the western section of the Canadian Arctic Archipelago (CAA), northern Alaska, Siberia, and northern Scandinavia. ICD was longer by ~1–4 weeks for Baffin Island, most parts of central to western Arctic Canada, southern Alaska, western Russia, and southern Scandinavia. Exceptions included: (1) Canadian lakes Amadjuak and Nettilling (the largest
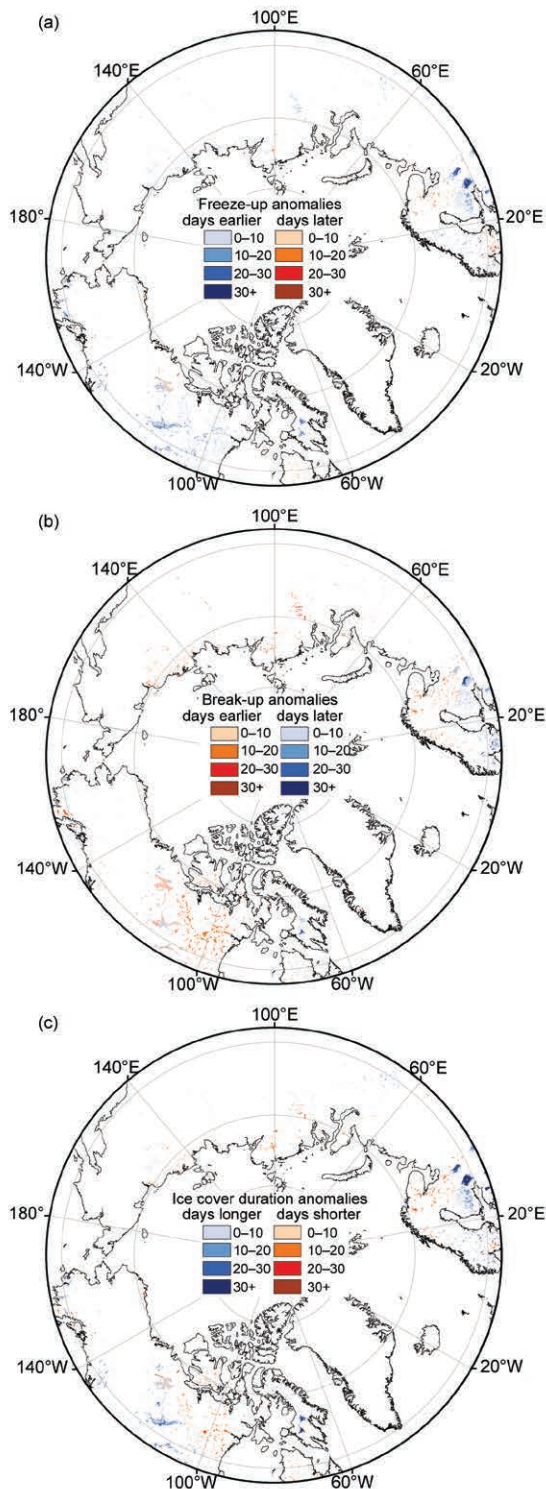
FIG. 5.26. (a) Freeze-up, (b) break-up, and (c) ice cover duration anomalies (in days) in the 2012/13 ice season relative to the 2004–12 average. Data are from the NOAA IMS (Helfrich et al. 2007) 4-km product, which incorporates a wide variety of satellite imagery, derived mapped products, and surface observations. Freeze-up and break-up dates, and ice duration were derived at the pixel level from this product.

lakes of Baffin Island) and Lake Hazen on Ellesmere Island, which experienced longer ICD by ~30–70 days; and (2) north European Lakes Onega and Ladoga (western Russia) by ~30–60 days, as well as smaller lakes to their south, and lakes in southern Norway. ICD for these smaller Russian and Norwegian lakes was longer by ~50–80 days in 2012/13 compared to the 2004–12 average.

l. Terrestrial permafrost—V. E. Romanovsky, S. L. Smith, H. H. Christiansen, N. I. Shiklomanov, D. A. Streletskiy, D. S. Drozdov, G. V. Malkova, N. G. Oberman, A. L. Kholodov, and S. S. Marchenko

Permafrost is defined as soil, rock, and any other subsurface earth material that exists at or below 0°C for two or more consecutive years. On top of the permafrost is the active layer, which thaws during the summer and freezes again the following winter. Average annual temperature of permafrost and the thickness of the active layer are good indicators of changing climate (Smith and Brown 2009). Increasing permafrost temperatures and active layer thickness caused by climate warming affect the stability of the northern ecosystems and infrastructure, and are predicted to cause the release of carbon into the atmosphere in the form of carbon dioxide (CO_2) and methane (CH_4; see section 5e). Here, permafrost temperatures and active layer thickness are reported for Alaska, Canada, Russia, and the Nordic region.

1) Permafrost temperature

In 2013, new record high temperatures at 20-m depth were measured at some permafrost observatories on the North Slope of Alaska (hereafter North Slope) and in the Brooks Range (Fig. 5.27a), where measurements began in the late 1970s and early 1980s (Fig. 5.27b). Changes in permafrost temperatures at 20-m depth typically lag about one year behind the changes in surface temperatures. The 20-m temperatures in 2013 were 0.03°C higher than in 2012 at West Dock and Deadhorse (Fig. 5.27b) on the North Slope and 0.06°C higher at Coldfoot (Fig. 5.27c) in the southern foothills of the Brooks Range. Permafrost temperatures in 2013 at the other North Slope sites were similar to those in 2012, except at Happy Valley where they were 0.06°C lower. Temperature at 20-m depth has increased between 0.28° and 0.47°C decade^{-1} since 2000 on the North Slope (Fig. 5.27b). Permafrost temperatures in Interior Alaska (Fig. 5.27a) continued to decrease in 2013 (Fig. 5.27c), a cooling that is due to a slight decrease in mean annual air temperature and lower than normal snow depth since 2007. Consequently, temperatures in 2013 at
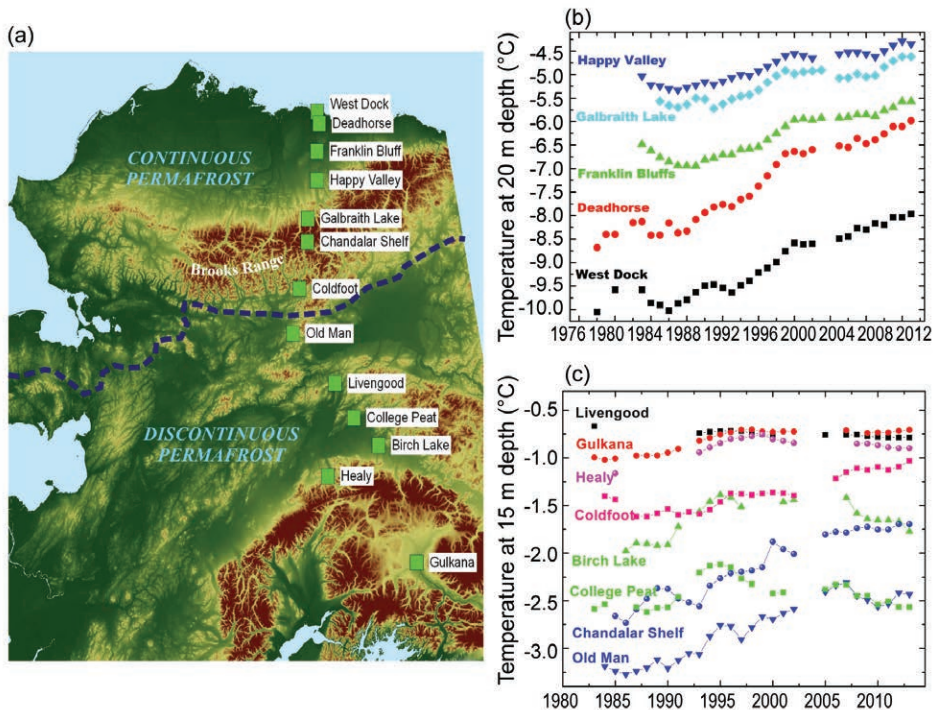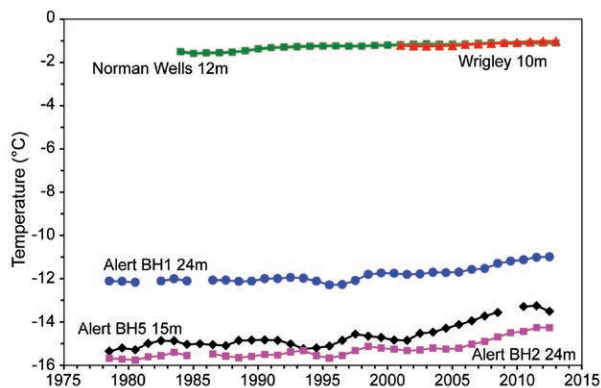
FIG. 5.27. (a) Map of Alaska showing the continuous and discontinuous permafrost zones (separated by the broken blue line) and locations of permafrost temperature measurement sites along a north–south transect. Time series of mean annual temperature (°C) at depths of (b) 20 m and (c) 15 m below the surface at the measurement sites (updated from Romanovsky et al. 2012).

aska Highway corridor in the southern Yukon and northern British Columbia. As a result, the southern limit of permafrost appears to have shifted northward by at least 25 km.

Permafrost temperature has increased by 1°–2°C in northern Russia during the last 30–35 years (Romanovsky et al. 2010b), similar to that observed in northern Alaska and the Canadian high Arctic. In the Polar Ural, for example, temperatures at 15-m depth have increased by ~0.5°C decade[-1] since the late 1980s at colder permafrost sites (Fig. 5.29, sites ZS-124, R-92, and R57). Less warming has been observed at warm permafrost sites and a slight cooling has occurred since 2009 (Fig. 5.29, sites ZS-124 and KT-16a).

some sites in Interior Alaska were lower than those located farther north, e.g., temperatures at College Peat and Birch Lake are now lower than at Old Man and Chandalar Shelf in the Brooks Range (Fig. 5.27).

In 2012/13, temperatures in the upper 25 m of ground at Alert, northernmost Ellesmere Island, Canada, were among the highest recorded since measurements began in 1978 (Fig. 5.28). At a depth of 15 m in borehole BH5, temperature has increased by ~1.4°C decade[-1] since 2000, which is almost 1°C higher than the rate for the entire record. Even at a depth of 24 m, temperature has increased since 2000 at a rate approaching 1°C decade[-1]. It should be noted, however, that over the last two years, the rate of temperature increase has slowed and there has been even a slight cooling at 15-m depth; this is likely a response to a decrease in air temperatures between 2010 and 2012. Temperatures in the warm permafrost in the central Mackenzie River valley in northwestern Canada continue to increase, but at a much slower rate that has slowed further in the last decade (Fig. 5.28). At depths of 10–12 m, the permafrost temperature at Norman Wells and Wrigley has risen by 0.07°–0.2°C per decade since 2000. A recent study by James et al. (2013) found that significant degradation of permafrost has occurred since 1964 along the Al-
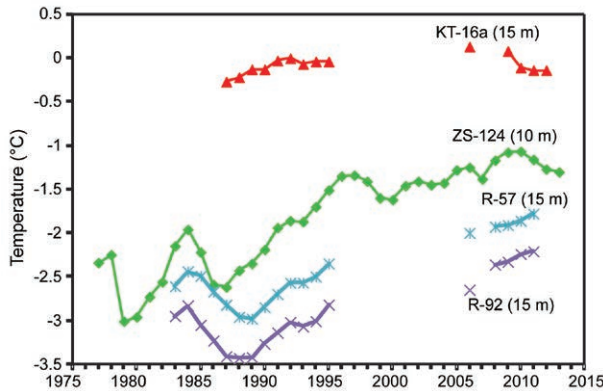

FIG. 5.28. Time series of mean annual permafrost temperatures (°C) at 10-m and 12-m depth at Wrigley (red squares) and Norman Wells (green squares) in the discontinuous, warm permafrost of the central Mackenzie River Valley, Northwest Territories, Canada, and at 15-m (black diamonds) and 24-m (two boreholes: blue circles and pink squares) depth in continuous, cold permafrost at Alert, Nunavut, Canada (updated from Smith et al. 2010, 2012). The method described in Smith et al. (2012) was used to address gaps in the data and produce a standardized record of mean annual ground temperature.

Fig. 5.29. Time series of annually-averaged permafrost temperatures (°C) at 10-m and 15-m depth at four research sites in the polar Ural, Russia.

There are limited long-term permafrost temperature records for the Nordic area. A few of these were initiated at the end of the 1990s and since then temperature has increased at rates of 0.4°–0.7°C decade[-1] in the highlands of southern Norway, northern Sweden, and Svalbard, with the largest warming in Svalbard and in northern Scandinavia (Isaksen et al. 2011; Christiansen et al. 2010). In western Greenland, permafrost temperatures are relatively warm, from −1° to −3°C (Christiansen et al. 2010). In eastern Greenland, the first full year of permafrost temperatures in 10 recently established boreholes (depth range of 2–18 m) were obtained in summer 2013, and the permafrost temperature was found to be −6° to −7°C.

2) Active layer thickness

Decadal trends in the active layer thickness (ALT) vary by region (Shiklomanov et al. 2012). In 2013, a majority of sites in Alaska reported higher ALT values relative to the 1995–2013 average, consistent with an exceptionally warm summer (see section 5b). On the North Slope, for example, ALT in 2013 was, on average, 11% higher than the 1995–2013 average of 0.47 m. The 2013 average ALT is 6% higher than in 2012 and on par with the 20-year maximum recorded in 1998. In Interior Alaska, ALT has been relatively unchanged since the maximum value reached in 2007, and 2013 values were slightly lower than in 2012. ALT in 2013 was similar to 2012 at sites on the Seward Peninsula, westernmost Alaska mainland.

A slight decrease in ALT in 2013 was observed in west Siberia a year after the highest values in the observational record were observed in 2012. This does not alter an observed thickening trend in west Siberia over the last six years. The 2013 ALT values are 8% higher than the 1995–2013 mean of 1.1 m. A more or less continuous thickening of the active layer has been reported at locations in the Russian European North, although ALT in 2013 was 6% lower than the record maximum of 2012. Central Siberian locations also report slightly lower ALT values in 2013 than in 2012. ALT in eastern Siberia in 2013 was similar to 2012, 10% lower than in 2011, and all sites had lower ALT than the 1996–2013 average of 0.64 m. In 2013, ALT values in Chukotka (Russian Far East) were about 2% higher than in 2012, marking a slight increase in ALT during 2011–13 following a sharp decline in 2008–10.